JOURNAL OF GEOPHYSICAL RESEARCH, VOL. 107, NO. B8, 2169, 10.1029/2001JB000548, 2002

Rotating thermal convection experiments in a hemispherical shell with heterogeneous boundary heat flux: Implications for the Earth's core

Ikuro Sumita
Department of Earth Sciences, Faculty of Science, Kanazawa University, Kanazawa, Ishikawa, Japan

Peter Olson
Department of Earth and Planetary Sciences, Johns Hopkins University, Baltimore, Maryland, USA

Received 30 March 2001; revised 13 December 2001; accepted 18 December 2001; published 23 August 2002.

[1] We report the results of thermal convection experiments in a rapidly rotating hemispherical shell with a heterogeneous heat flux at the outer boundary to model the effect of a thermally heterogeneous core-mantle boundary on the convection in the Earth's outer core. A parameter study is made by varying the heat flux, size, and location of an anomalously heated patch for a range of Rayleigh numbers at $\sim 10^8$ and a fixed Ekman number 4.7×10^{-6}. Experiments show that fully developed, boundary-driven convection occurs when the radial convective heat transfer from the heater exceeds that of the surrounding boundary region. The flow consists of a large-scale cyclonic circulation originating from the heater and includes a radially extending spiralling front with a jet. The front is stationary when the sectorial high heat flux region is imposed at low latitudes but becomes unstable when it is imposed at high latitudes. The ratio of applied heat which is partitioned to radial and lateral heat transfer becomes fixed in this regime. Measurements also indicate that there is a close correlation between the flow direction and the statistics of temperature fluctuations. Applied to the Earth, the experiments suggest that there are two scales of flows in the core: fine-scaled jets and slower, large-scale flows. The large-scale hemispherical structure of the core can be interpreted in terms of the boundary-driven flow driven by the high heat flow region beneath east Asia. *INDEX TERMS:* 8115 Tectonophysics: Core processes (1507); 7207 Seismology: Core and mantle; 8121 Tectonophysics: Dynamics, convection currents and mantle plumes; 8130 Tectonophysics: Evolution of the Earth: Heat generation and transport; 8180 Tectonophysics: Evolution of the Earth: Tomography; *KEYWORDS:* core-mantle boundary, heat flux heterogeneity, outer core, inner core, thermal convection experiment, rotating spherical shell

1. Introduction

[2] Compositional and thermal buoyancy acquired at the inner core boundary is generally considered to be the primary source which drives the convective motions in the Earth's core [e.g., *Buffett*, 2000]. There is another important source of flow, which is the lateral variation of heat flux at the core-mantle boundary (CMB) imposed by the mantle. Because the core flows faster than the mantle by about 5 orders of magnitude, the core responds to the thermal heterogeneity imposed by the mantle, and a boundary-driven flow is induced in the core. There are several observational evidence which suggest that such boundary-driven flow is important in the outer core. The time-averaged geomagnetic field pattern and its secular variation include a nonaxisymmetric part [e.g., *Bloxham and Gubbins*, 1987; *Bloxham et al.*, 1989; *Walker and Backus*, 1996; *Johnson and Constable*, 1998] and the core flow inferred from the field show longitudinal variation [e.g., *Bloxham*, 1992]. The inner core seismic structure, which records how the inner core solidifies from the outer core [*Sumita et al.*, 1996; *Yoshida et al.*, 1996; *Bergman*, 1997; *Bergman et al.*, 2000], also exhibits longitudinal variation [e.g., *Tanaka and Hamaguchi*, 1997; *Creager*, 1999, 2000; *Garcia and Souriau*, 2000, 2001; *Niu and Wen*, 2001]. Since inner core solidification is ultimately controlled by the heat transfer in the outer core, the inner core heterogeneity suggest that the lateral variation of outer core heat transfer may extend as deep as to the inner core boundary.

[3] Previous studies on the effect of thermally heterogeneous boundary condition on convection in rotating spherical shells can be classified into the following categories. Category A is convection without a magnetic field and can be subdivided into category A-1, in linear or weakly nonlinear regime, [*Zhang and Gubbins*, 1992, 1993, 1996; *Yoshida and Hamano*, 1993; *Yoshida and Shudo*, 2000; *Gibbons and Gubbins*, 2000], and category A-2, in strongly

0148-0227/02/2001JB000548$09.00

nonlinear regime [*Sun et al.*, 1994; *Sumita and Olson*, 1999]. Category B is convection with magnetic field and can be subdivided into category B-1, the case without inertia (magnetoconvection [*Yoshida and Hamano*, 1993] or self-consistent mean field dynamo [*Sarson et al.*, 1997]), and category B-2, the case with inertia (magnetoconvection [*Olson and Glatzmaier*, 1996] or fully self-consistent dynamo [*Glatzmaier and Roberts*, 1997; *Glatzmaier et al.*, 1999; *Bloxham*, 2000a, 2000b]). Note that the imposed boundary conditions differ among these studies. Various combinations of imposed temperature or heat flux with differing patterns and amplitude of heterogeneity, stress-free or no-slip velocity conditions are used. The mean state also differs; for example, it can be stratified, convective, with or without heat sources, under different Ekman, Rayleigh, and Prandtl numbers. These differences complicate efforts to draw general conclusions from the results of these studies.

[4] Category A-1 is the simplest case, and the solutions show that the downwelling region is shifted eastward relative to the low-temperature or high heat flux region at the core-mantle boundary. The fluid mechanics for this phase shift is relatively well understood (see section 4.2.2). A situation more relevant to the core is to include the effects of magnetic field and fluid inertia (turbulence). Results of the numerical calculations including both magnetic field and fluid inertia (category B-2) are quite complicated and difficult to understand in terms of basic force balances. Therefore it is worth considering these effects separately at first. For numerical calculations, including a magnetic field is easier to achieve because spatial scales of convection are larger. On the other hand, experiments are better suited if turbulence with fine-scaled and rapidly varying flows are important.

[5] The experiments by *Sumita and Olson* [1999] were made in the following parameters: $Ek = 4.7 \times 10^{-6}$, $19 < Ra/Ra_c < 52$ ($Ra_c = 1.8 \times 10^7$), which is further into the regime of geostrophic turbulence than previous numerical calculations, for example, by *Sun et al.* [1994], which used $Ek = 6.3 \times 10^{-4}$, $Ra/Ra_c = 5$ ($Ra_c = 3.6 \times 10^4$). Here, Ek is the Ekman number, and Ra is the Rayleigh number (Ra_c is the critical Rayleigh number). *Sumita and Olson* [1999] used a localized heater attached to the outer sphere and studied how the convective pattern changes with heating. They found that a fully developed, boundary-driven convection forms for a sufficiently large heat flux contrast. They proposed a model of flow and heat transfer in the outer core that is compatible with the flow inferred from geomagnetic secular variation and the longitudinally heterogeneous seismic structure of the inner core.

[6] In this paper, we report the results of the detailed parameter study of the boundary-driven convection. In addition to heat flux we investigated how the boundary-driven convection changes with Rayleigh number, heater size, and its location. We also report detailed measurements of convective pattern, flow velocity, temperature, and global heat flow. These are analyzed and interpreted using a columnar convection model and applied to the boundary-driven convection in the Earth's core. This paper is made up as follows. We describe the experimental method (section 2), followed by the results and their analysis (section 3). We model the experimental results (section 4), and a comparison is made with previous numerical calculations (section 5). Finally, we apply our results to Earth's core (section 6).

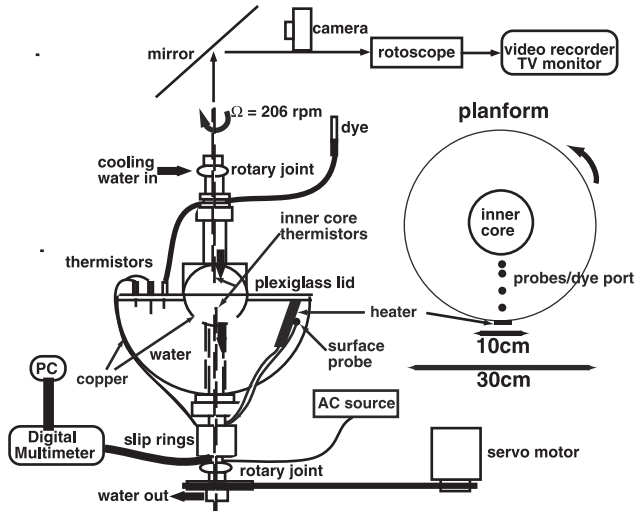

Figure 1. Sketch of the experimental apparatus.

2. Experimental Method

[7] The experimental apparatus is shown in Figure 1. This type of apparatus for studying convection in rotating spherical shells was first used by *Busse and Carrigan* [1976]. The details of this apparatus are given by *Sumita and Olson* [2000], and we describe only the essential and new features below. A hemisphere of an outer diameter of 30 cm and an inner diameter of 10 cm is spun at 206 rpm. A temperature difference is imposed across the shell to initiate thermal convection by cooling the inner core. The convective pattern is visualized by Kalliroscope flakes. The temperature within the fluid is measured by thermistor probes. These probes sample at intervals of 1 s. Hypodermic types are positioned at distances of 1.5, 3.1, 5.6, and 8.1 cm from the inner core boundary near the equatorial plane, and surface types are attached at the core-mantle boundary (at latitude = 10°, adjacent to the heater and at its antipode). The velocity is determined from the video recordings of the motion of tracer dyes. Strip heaters of various sizes and shapes are attached to the core-mantle boundary controlled by an AC power source to impose a localized anomalous heat flux. The outer surface of the heater is thermally insulated, and the radially outward heat loss is estimated to be negligible compared to that directed inward. A certain fraction of the applied heat is lost laterally along the core-mantle boundary by conduction along the copper hemisphere and from lateral convective heat transfer. The total heat flux at the inner core boundary is measured by the temperature rise of the circulating water. Other experimental conditions are summarized in Table 1.

[8] The experimental procedure is as follows. We first achieve an equilibrium convective state without heating and then apply the heterogeneous heating to achieve a new equilibrium state. The new thermal equilibrium state is achieved typically in several zonal circulation times (~3 hours) and is monitored by visually observing the convective pattern, temperature measurements at the outer boun-

Table 1. Parameters

Parameter	Experiments	Earth's Core[a]
Inner/outer radius ratio R_{ICB}/R	0.33	0.34
Prandtl number Pr, ν/κ[b]	7	0.01
Ekman number (Ek), $\nu/\Omega D^2$[c]	4.7×10^{-6}	$\sim 10^{-15}$
Rayleigh number Ra, $\alpha g \Delta T D^3/\kappa\nu$[d]	$-2.6 \times 10^8 \sim 7.5 \times 10^8$	$>10^{20}$[e]
Ra/Ra_c	$-15 \sim 44$[f]	$\sim O(10)$?[g]
Q_{active}/Q_{quiet}[h]	<2	~2?
q^*[i]	<100	<100?
$\Delta T_{CMB}/\Delta T$[j]	<4	1–10?

[a] Molecular values used for material properties.
[b] The ν is kinematic viscosity, κ is thermal diffusivity.
[c] Ω is rotation rate, D is shell thickness.
[d] The α is thermal expansivity, $g(\Omega) = D\Omega^2$ for experiments, ΔT is superadiabatic temperature difference across the shell.
[e] Corresponds to Ra_c for a nonmagnetic thermal convection estimated using an asymptotic solution of *Jones et al.* [2000].
[f] $Ra_c = 1.8 \times 10^7$ [*Sumita and Olson*, 2000].
[g] Estimated as $\Delta T \sim 10^{-5}$ K, which corresponds to an average convective heat flux for $Q_{CMB} = 3 \times 10^{11}$ W.
[h] Q_{active}, Q_{quiet}, total radial heat flow in the active and quiet regions.
[i] The q^* is applied heat flux at heater divided by the average heat flux at CMB.
[j] ΔT_{CMB} is lateral temperature variation at CMB, which is the temperature adjacent to heater minus the temperature at antipode of heater.

dary and in the fluid, and heat flux measurements at inner core boundary. After each set of measurements a stepwise increase or decrease of the heater output was made, and the system was allowed to come to a new equilibrium.

3. Experimental Results

[9] Under a homogeneous boundary the flow is characterized by 2-D plumes that are advected westward by the mean zonal flow (geostrophic turbulence) [*Sumita and Olson*, 2000]. We first describe the results of a parameter study of convection under a thermally heterogeneous boundary under a fixed Ekman number 4.7×10^{-6}, followed by a detailed study of these flows.

3.1. Parameter Dependence of Convective Pattern

3.1.1. Heat flux dependence

[10] In Figure 2 we show how this convective pattern and flow change as the strength of the heater is increased at $Ra/Ra_c \simeq 26.3 \pm 2.1$ and $Ek = 4.7 \times 10^{-6}$. Here the heater covers a latitudinal range of 0–48° and a longitudinal range of $\Delta H_\phi \simeq 9.7°$. We measure the magnitude of the heat flux heterogeneity using Q^* defined as

$$Q^* = \frac{\text{Applied total heat flow}}{\text{Total heat flow at inner core boundary}}, \qquad (1)$$

because we found this to be the main parameter which governs the convective regimes from varying the Rayleigh number and heater size (sections 3.1.4 and 3.1.5). The total anomalous heat flow is calculated from the applied current and voltage of the heater. Some fraction of heat is lost laterally, so this represents an upper bound for the total heat that enters the fluid.

[11] We find two convective regimes as the heat flux is increased: First, there is a local locking regime, for $Q^* <$ 0.7. This is a regime intermediate between the regimes of convection under a homogeneously heated boundary and the fully developed boundary-driven convection (Figure 2a). Second, there is a global locking regime for $Q^* >$ 0.7. This appears to be an asymptotic regime for fully developed boundary driven convection (Figures 2b, 2c, and 2d), and a schematic diagram of the flow pattern is shown in Figure 3. We describe the details for each of these regimes below.

3.1.2. Local locking regime

[12] The convective pattern in the local locking regime is illustrated in Figure 2a, visualized by flakes. The convection beneath the heater has the same general structure as the convection under the thermally homogeneous boundary. However, dye injected near the heater is transported in the prograde direction, revealing a localized eastward flow adjacent to core-mantle boundary. This flow transports heat in the prograde sense and results in a higher fluid temperature to the east of the heater compared to the fluid to the west. The depth extent of the eastward flow increases with the strength of the anomalous heating.

3.1.3. Global locking regime

[13] In the global locking regime the anomalous heating generates a spiralling structure that extends radially across the entire spherical shell, as shown in Figures 2b, 2c, and 2d. The spiral structure, a stationary front separating relatively warm fluid to the west from relatively cold fluid to the east, originates from the core-mantle boundary region eastward of the heater. In addition to the large temperature difference across the front (Figure 4) there is also strongly concentrated flow. Dye motion indicates that the eastward flow along the core-mantle boundary originating from the heater converges to form into a narrow jet, with a width of ~4 mm. The jet flows from the core-mantle boundary to inner core boundary along the temperature front. Fluid motion in the jet is nearly geostrophic; as seen from an oblique view in Figure 5, the front forms a 2-D curtain aligned parallel to the rotational axis. With increased heating, the temperature difference across the front increases and the terminus of the front shifts eastward on the inner core boundary, while the origin of the jet on core-mantle boundary shifts slightly westward, until it becomes pinned at about ~50° east of the heater.

[14] In summary, the convection pattern in the global locking regime consists of two distinct fluid regions, separated by a sharp front with a strong thermal gradient. East of the heater and west of the front is a relatively warm region with a large-scale cyclonic circulation, and east of the front is a relatively cold region with a westward flow as shown in Figure 3.

3.1.4. Rayleigh number dependence

[15] The regimes described above are affected by the Rayleigh number of the background convection. In Figure 6a we show the convective pattern at $Ra/Ra_c \simeq 62$, a higher Rayleigh number than the images in Figure 2. Note that the convective pattern in Figure 6a is similar to Figure 2c, even though the applied heating in Figure 6a is 2.6 times larger. For comparison, the background heat flow (without the anomalous heater) is larger in this case than in the case shown in Figure 2. The similarity of flow structures in Figures 6a and 2 shows that in order to preserve the same

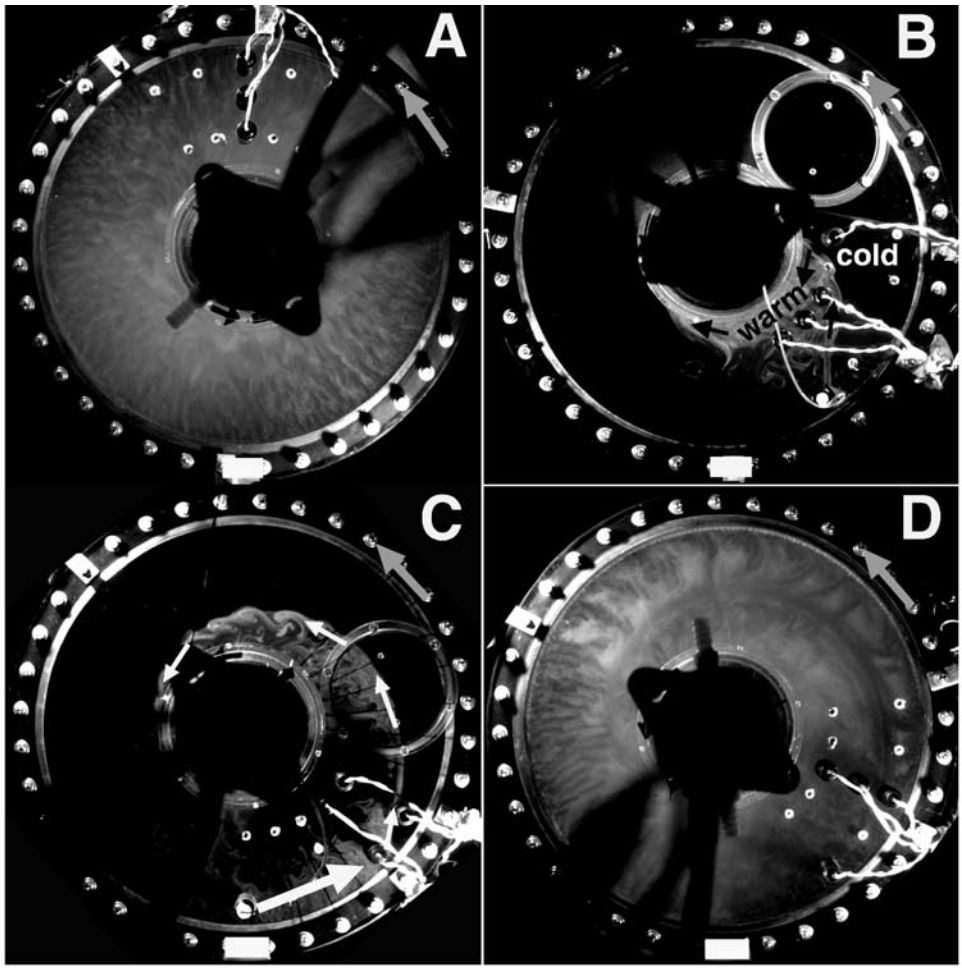

Figure 2. Convective patterns in the equatorial plane visualized by flakes (Figures 2a and 2d) and fluorescent dye (Figures 2b and 2c). In all cases, $Ra/Ra_c = 26.3 \pm 2.1$ ($\Delta T = 6.84 \pm 0.56$°C). The white rectangle indicates the heater location. Its dimensions are 0–48° in latitude, 0–9.7° in longitude. Cases in Figures 2a–2d represent increasingly heterogeneous heat flow. The parameters of each case are (a) $Q^* = 0.45$ ($q^* = 20$), $\Delta T_{CMB} = 1.48$°C; (b) $Q^* = 1.10$ ($q^* = 48$), $\Delta T_{CMB} = 6.21$°C; (c) $Q^* = 1.57$ ($q^* = 69$), $\Delta T_{CMB} = 7.53$°C; (d) $Q^* = 2.17$($q^* = 95$), $\Delta T_{CMB} = 12.82$°C. (Note that Q^* is defined in equation (1); q^* is heat flux at heater divided by average heat flux at CMB; ΔT_{CMB} is temperature adjacent to heater minus temperature at antipode of heater.) White and black arrows indicate the flow directions. Rotation is counter clockwise in these views.

convection structure, the anomalous heating must be increased in conjunction with the background heat flow.

[16] Figure 6b shows the convective pattern at $Ra/Ra_c = -2.4$, corresponding to a stably stratified background temperature profile. We find in this case that a front forms to the east of the heater, as in the convectively unstable cases. However, in this case the stable stratification suppresses the radial extent of the front. Dye motion indicates that the pattern of flow in the general circulation is essentially the same as with a convective mean state. Radial temperature profile measurements indicate that in the region with boundary-driven flow (i.e., east of the heater) the stable thermal stratification is destroyed. In the regions that are less affected by boundary-driven flow (i.e., west of the heater) the stable stratification persists.

3.1.5. Heater size dependence

[17] In order to clarify whether the heat flux or the total heat flux controls the convective regimes, we compare the experiments with different heater size but same total heat flow. Figures 7a and 7b show the convective patterns obtained using two heaters with the same latitudinal range of 0–48° but different longitudinal ranges, $\Delta H_\phi \simeq 9.8°$ and $\Delta H_\phi \simeq 40°$, respectively, both at $Ra/Ra_c \simeq 35$. The total heat flow at the heater is the same in these two cases, although the local heat flow anomaly in Figure 7a is 4 times larger than in Figure 7b. Comparison of Figures 7a and 7b shows that the convective pattern are essentially the same. The temperature difference across the front is also similar (see Figure 7 caption). This demonstrates that total heat flow anomaly (and not the local heat flow anomaly) is the main parameter which governs the convective pattern.

3.1.6. Effects of the pattern of heat flow anomaly

[18] The pattern of the heterogeneity is another important parameter controlling boundary-driven convection. Here we describe the results of three different heater locations and

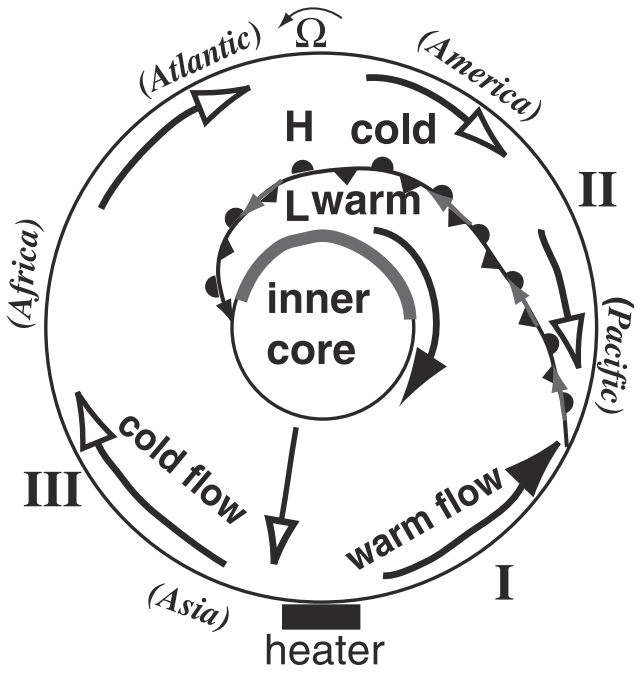

Figure 3. A schematic diagram of the flow pattern in the global locking regime. The stationary temperature front separates the high-pressure cold region and low-pressure warm region. The gray arrows indicate the jet along the front. The shaded area on the inner core boundary is the inferred high heat flow region produced by the inward spiralling jet. Warm and cold fluid is indicated by black and white arrow heads, respectively. The names in parentheses correspond to the experimental model of the Earth's core [*Sumita and Olson*, 1999]. The sense of temperature needs to be reversed when applying to the Earth's core.

then generalize our results to infer the behavior of complicated heating patterns.

[19] First, we examine how the latitudinal range of applied heating controls the results by considering two cases using the same heater used in Figure 2 but positioned at low and high latitudes, respectively. When the heater was attached at low latitude covering 0–9.7° and a longitudinal range of $\Delta H_\phi \simeq 48°$, we find that the front does not traverse across the shell but becomes diffuse near the inner core boundary. We interpret this as a consequence of diminishing lateral temperature variation near the inner core boundary because the heterogeneous heating is absent at high latitudes.

[20] When the same heater is attached at high latitude covering a latitude of 50.1–59.9°, and a longitudinal range of $\Delta H_\phi \simeq 60°$, we find that a front-like structure forms initially in response to this heating pattern, but it does not persist for long. Evidently, high-latitude heating does not create the large pool of warm fluid near the equator that is necessary to sustain strong eastward flow there. Figure 8 shows temperature records for this case at two locations with the same distance from the inner core boundary. The long-period (~20 min) oscillation of the temperature records corresponds to the periodic formation and destruction of the front. This cycle of front formation and erosion is confirmed by observing the changing dye patterns. During the portion of the cycle when the front is eroded, cold fluid crosses the front and enters the warm region from the east. This effect is seen in the temperature records, which show a decrease first at probe A and later at probe B. The phase difference between the two probes is ~400 s and corresponds to a westward flow velocity of 3×10^{-4} m s^{-1} at this region of the fluid.

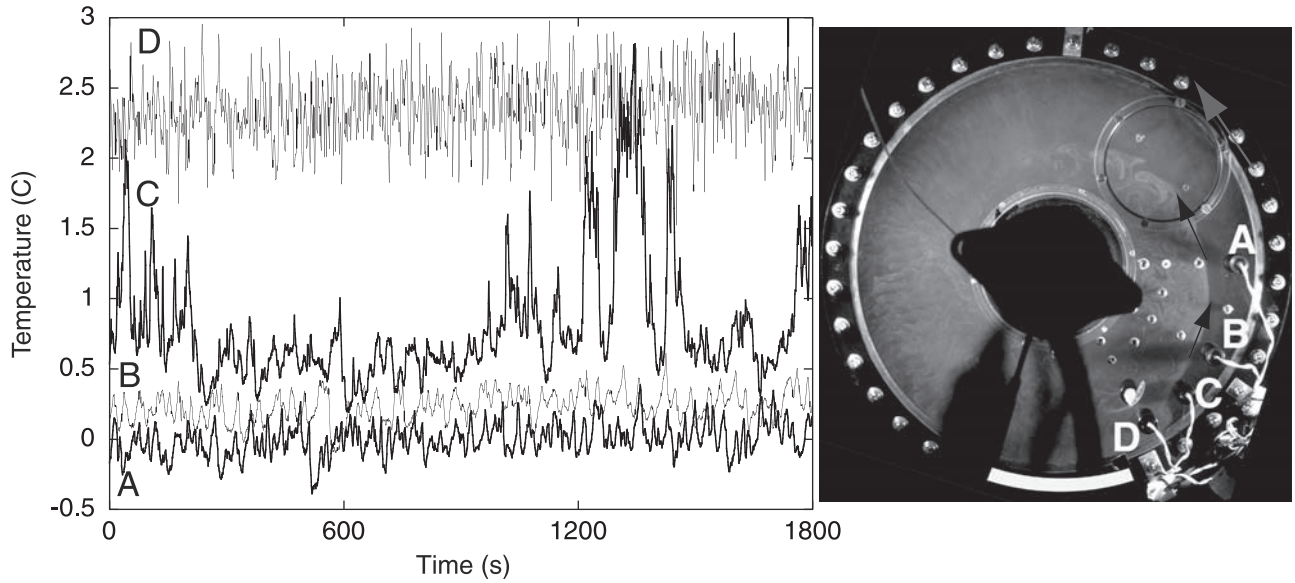

Figure 4. Temperature recorded at the prograde and retrograde sides of the front for the case with $Ra/Ra_c = 39.4$ ($\Delta T = 10.23$°C), $\Delta T_{\mathrm{CMB}} = 12.25$°C, $Q^* = 1.5$ ($q^* = 17$). The records show the difference between each probe and the mean temperature at probe A, which is used as the reference temperature. In the dye image the heater is indicated by a white band, covering latitude 0–48°, longitude range 40°, and the probe locations are shown. Probes A, B, C, and D are located 8.1 cm from the inner core boundary at longitudes 90, 60, 45, and 30°, respectively, prograde from the center of the heater. The trajectory of the jet is indicated by black arrows.

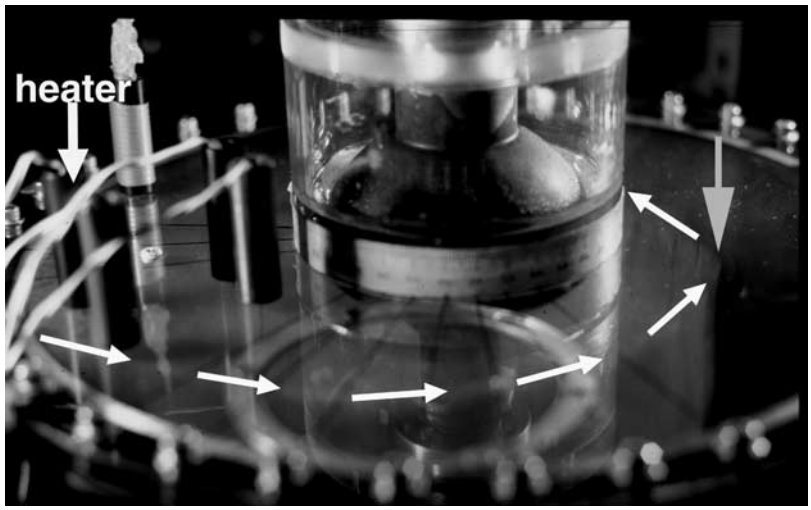

Figure 5. An oblique view of the stationary temperature front visualized using fluorescent dye for the case shown in Figure 2c. White arrows indicate the trajectory of the 2-D jet flowing from the core-mantle boundary to inner core boundary. A gray arrow indicates the dye curtain. Rotation is left to right in this view.

[21] The second geometry that we examine is a zonal heterogeneity in boundary heating. Zonal heating is produced by attaching a heater around the equator of the outer hemisphere, covering a latitude band between 0 and 10°. The zonal heating also results in eastward flow, but in this case, no front was observed. Dye images indicated that the 2-D plumes generated at the outer boundary are sheared by the zonal flow, as for other heating patterns. We observe a change in the mean zonal flow as the heater strength is changed. For a heating strength $Q^* \sim 1.4$ a relatively weak eastward flow induced by the heater coexists with the stronger background westward flow. Increasing the heater strength to $Q^* \sim 1.7$ causes the eastward flow to become dominant. There are other differences between this case and homogeneous heating. For large Q^*, where the eastward flow predominates, the amplitude and frequency of temperature fluctuation becomes nearly independent of radius. This contrasts with the case of homogeneous boundary heating, where the temperature fluctuations are largest near the inner core boundary. The thermal structure in the axial direction also reverses with Q^*, becoming warmer in the equatorial plane. We also find that the skewness of the time derivative of temperature is negative near the inner core boundary but becomes positive near core-mantle boundary. Since a positive derivative is associated with eastward flow (section 3.2.2), this result indicates that the eastward flow becomes stronger near the core-mantle boundary.

[22] The third geometry we consider is two identical heaters, the same used in Figure 2, attached to the boundary at antipodal locations. In this case we observe two fronts, separated in longitude by 180°, as expected. However, the eastward spiral trajectory of the front is reduced in this case, compared to single heater cases. Instead of spiralling around the inner core, the two fronts are confined to within 180° of their respective heaters. The leading edge of the front becomes diffuse near the inner core boundary, resulting in a decreased lateral temperature difference there, compared to single heater cases. This indicates that with higher wave number boundary heating, there would be a greater tendency for the fronts to form directly beneath the high heat flow areas.

3.2. Detailed Description of a Boundary-Driven Convection

[23] In this section we describe the details of boundary-driven convection for the case when a heater was attached at a latitudinal range of 0–48° and a longitudinal range of $\Delta H_\phi \leq 9.7°$.

3.2.1. Flow structure: Global locking

[24] When a dye is injected adjacent to the heater, we observe the following sequence of flow structures in the cases with global locking. First, we observe an eastward flow adjacent to the core-mantle boundary (Figure 9a). The depth extent of this flow is about 1.5 cm. This depth scale appears to be independent of the heater strength Q^* and, as far as we could detect, independent of the size of the heater. Radially oriented plumes emerge from the core-mantle boundary at the heater, and as these plumes develop, they become advected and sheared by the eastward flow. The eastward deflection of the plumes is an indication that the zonal flow is faster than the radial flow in this region.

[25] Dye trajectories reveal that the eastward flow feeds into the jet, which separates from the core-mantle boundary and traverses the fluid shell along an eastward spiralling front that extends from core-mantle boundary to inner core boundary (Figure 9b). The jet decelerates as it nears the inner core boundary. As the front becomes fully developed, dye from the jet becomes entrained into an array of cyclonic vortices that emerge from the west side of the jet. The initial stage of the formation of these cyclones can be seen in Figure 9b, which develop to those seen in Figure 2c. The origin of these secondary cyclones is uncertain; however, because a large shear is present at the jet, they may represent Kelvin-Helmholtz instabilities of the laminar jet structure. As the jet approaches the inner core boundary, fluid from the jet mixes with the fluid in the region west of the front, and is deflected westward, forming a large-scale cyclonic circulation. On the other hand, in the region of westward

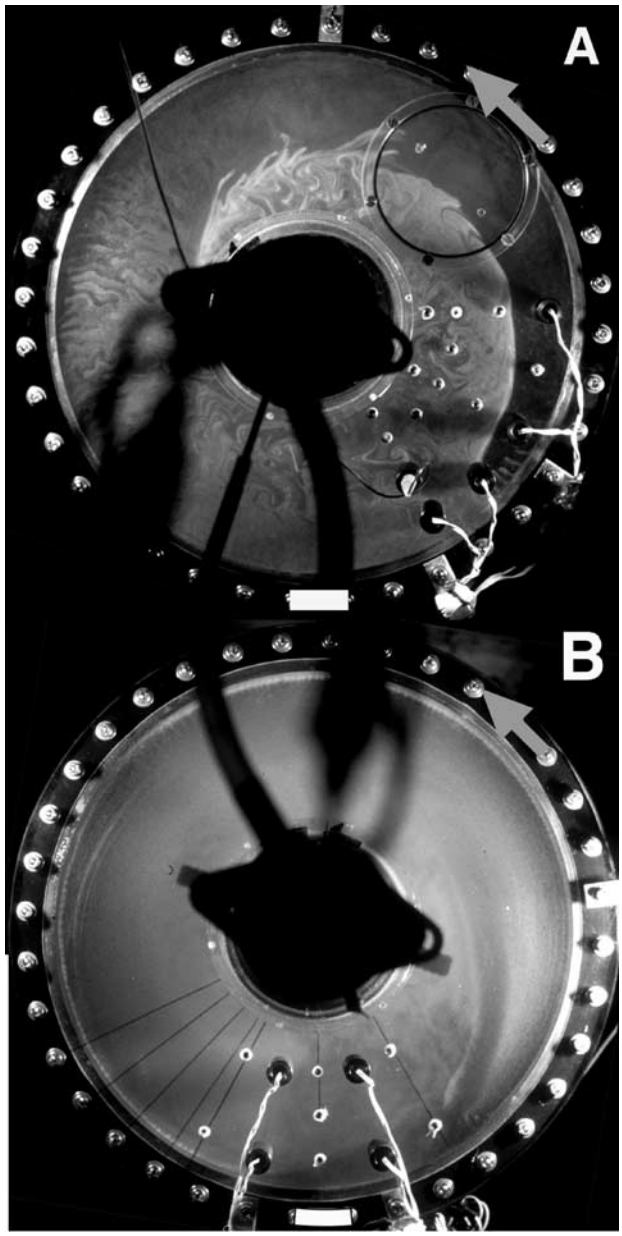

Figure 6. Convective patterns in the globally locked regime at different Rayleigh numbers. (a) High Rayleigh number case, $Ra/Ra_c = 61.8$ ($\Delta T = 16.05°C$), $Q^* = 1.17$($q^* = 51.02$), $\Delta T_{CMB} = 22.18°C$; (b) stably stratified case, $Ra/Ra_c = -2.4$ ($\Delta T = -0.63°C$), $Q_{ICB} \simeq 0$ W, $Q_{applied} \simeq 25$ W, $\Delta T_{CMB} = 9.77°C$. Location of the heater, shown by white rectangle, is the same as in Figure 2.

flow, we find that the warm plumes are attached to the core-mantle boundary (Figures 9d and 9e). In the region wedged between the front and the core-mantle boundary, these plumes are observed to have a long-wavelength modulation for every $\sim 10°$ in longitude, forming bundles of plumes (Figure 9c).

[26] As the lateral variation of temperature becomes larger with increasing Q^* and higher Rayleigh numbers, the velocity of the eastward flow and the jet becomes faster, and the timescale of mixing becomes shorter, but otherwise the flow pattern and the sequence of development remains the similar. Since the basic flow structures described here occur over a range of Rayleigh numbers, we suggest that this form of globally locked convection represents an asymptotic state of heterogeneous boundary-driven convection in a spherical shell geometry.

[27] There is evidence for ageostrophic components of the flow. When the dye is introduced into the west side of the front, hardly any dye is seen to mix across the front. On

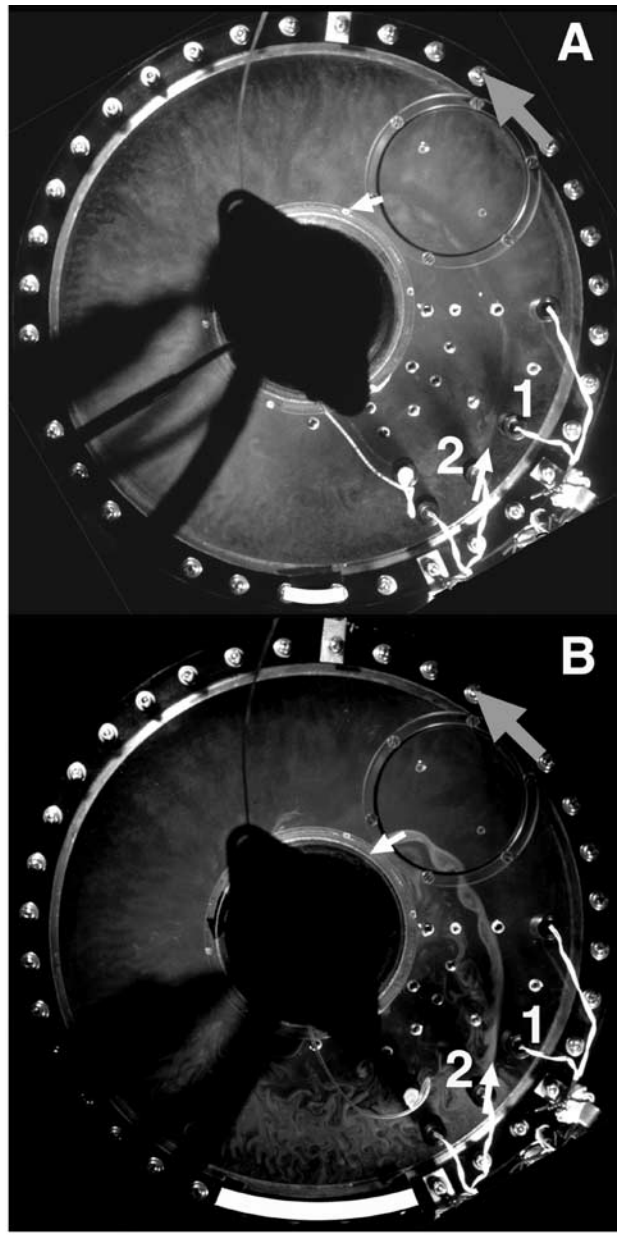

Figure 7. Comparison of convective patterns at $Ra/Ra_c = 35.2 \pm 0.0°C$ ($\Delta T = 9.16 \pm 0.0°C$). Each case has the same total applied heat flux but differing heater size (latitude range 0–48°; differing longitude range ΔH_ϕ). Temperature across the front $\Delta T_{front} = T_{probe2} - T_{probe1}$. (a) $\Delta H_\phi = 10°$, $Q^* = 1.30$ ($q^* = 57$), $\Delta T_{CMB} \simeq 10.9°C$, $\Delta T_{front} = 1.68°C$; (b) $\Delta H_\phi = 40°$, $Q^* = 1.21$ ($q^* = 13$), $\Delta T_{CMB} \simeq 9.17°C$, $\Delta T_{front} = 1.50°C$.

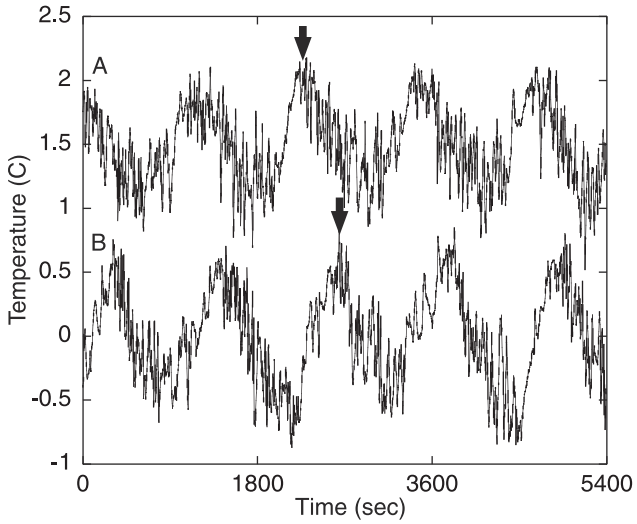

Figure 8. Temperature records at Ra/Ra_c = 40.7 (ΔT = 10.58°C), for the case of heterogeneous heating at high latitudes. The heater is attached at latitude = 50.1–59.9° and longitudinal range ΔH_ϕ = 60°. Thermal heterogeneity parameters are Q^* = 1.49(q^* = 65). The temperature record from probe A has been shifted upward by 1.5°C for clarity. Both probes are located in the equatorial plane, 8.1 cm from the inner core boundary. The longitudes of probes A and B are 95° and 35° east of the heater, respectively. The arrows indicate the phase difference between the two probes of the long-period oscillation.

the other hand, when the dye is introduced into the east side of the front, we observe dyed fluid slowly penetrating into the region west of the front. We interpret this behavior in terms of an axial component of flow (flow parallel to the spin axis of the spherical shell), which pumps the fluid from the region east of the front to the west. According to this interpretation, the warm fluid region behaves as a low-pressure system.

[28] The dye images also reveal several different length scales are present in the flow. Two in particular deserve special note. The important short length scale corresponds to the width of high-gradient structures, such as the transverse width of the plumes and the jet. This scale is ~4 mm in our experiments. The important large length scale is defined by the dimensions of the scale of the large-scale circulation, measured in the equatorial plane. This scale also corresponds to the longitudinal dimension of the front and is ~10 cm in our experiments.

3.2.2. Thermal structure of globally locked convection

[29] Figure 10 shows the isotherms in the equatorial plane under global locking, constructed from discrete temperature measurements by thermistor probes at several locations in the fluid. From the characteristics of the isotherms and the flow pattern shown in Figure 3, we define two sectors at the region beneath core-mantle boundary, separated by the front. These sectors are as follows:

1. The active sector contains warm fluid with an eastward flow beneath core-mantle boundary and is characterized by large radial heat transfer. In this region

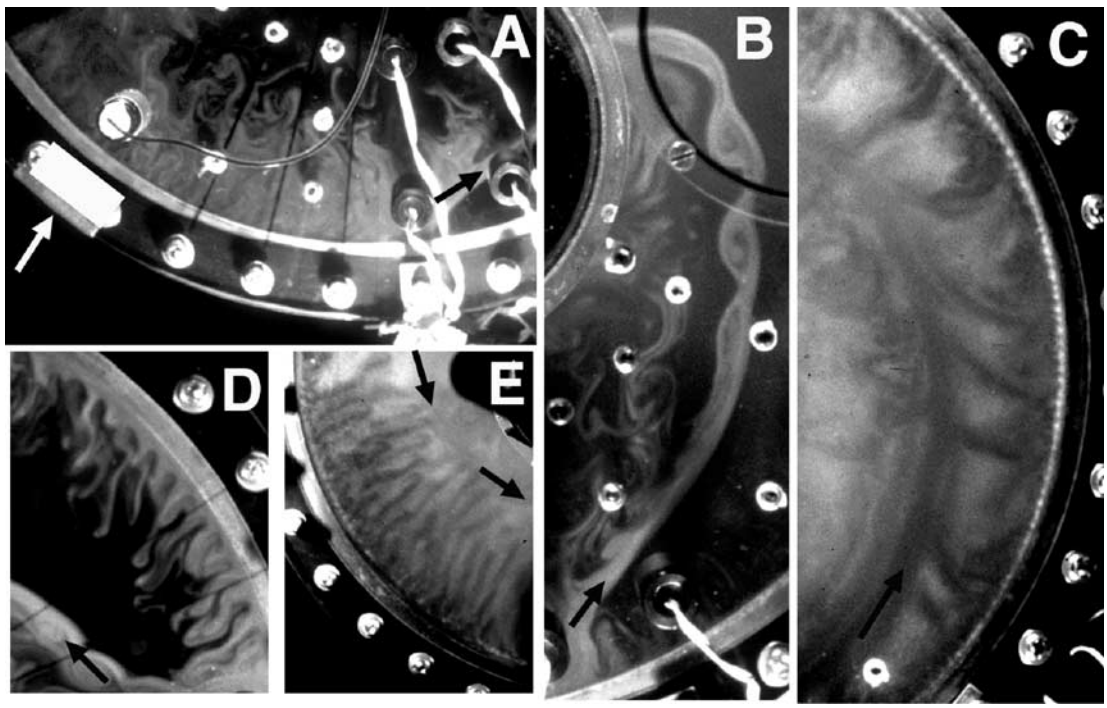

Figure 9. Close-up images of several types of flow structures. Black arrows indicate the flow direction in the jet along the front. The white arrow indicates the heater location. The location of the heater is the same as in Figure 2. (a) Detail from Figure 2c, showing eastward flow originating near the heater. (b) Detail from Figure 7b, showing the jet with billows. (c) Detail from Figure 2d, showing the modulation of warm plumes in region II of Figure 3. (d) Detail of the warm plumes imaged by dye in region II of Figure 3. Ra/Ra_c = 19.3 (ΔT = 5.02°C), Q^* = 1.06 (q_* = 46.5), ΔT_{CMB} = 7.36°C. (e) Detail from Figure 2d showing the warm plumes in region III of Figure 3.

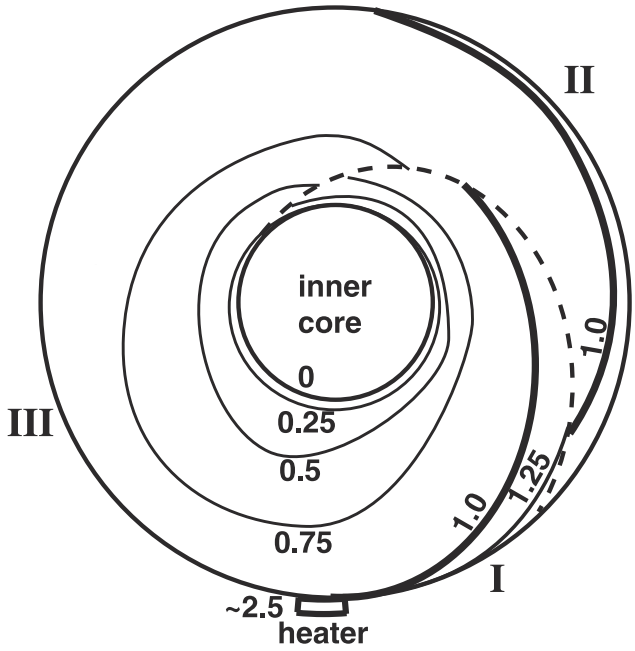

Figure 10. Isotherms in the equatorial plane in the global locking regime, reconstructed from temperature measurements at discrete points in the fluid. Here the temperature is normalized by ΔT, the temperature difference between the inner core boundary and core-mantle boundary (antipodal of heater). The "$\sim$2.5" indicates the temperature at the outer sphere adjacent to and west of the heater. The dashed line indicates the front.

(region I of Figure 10), we observe $\partial T/\partial\phi > 0$, $\partial T/\partial r > 0$, plus large amplitude and frequency of temperature fluctuations (T').

2. The quiet sector contains cold fluid with a westward flow and is characterized by a small radial heat transfer. This region is further subdivided according to region II, with $\partial T/\partial\phi < 0$, $\partial T/\partial r \geq 0$, small amplitude and frequency of T', and region III, with $\partial T/\partial\phi \sim 0$, $\partial T/\partial r > 0$.

[30] The eastward increase of temperature in region I is characteristic of rotating convection. In nonrotating convection we would expect the temperature to decrease with distance from the heater, instead of the increase we observe here. The isotherms near the inner core boundary in region I at the immediate west of the front are closely spaced, which indicates that the conductive heat transfer in the thermal boundary layer adjacent to inner core boundary is large there.

[31] The temperature structure in cases with local locking are similar to those with global locking, but in general, the thermal anomalies are confined more to the region near the core-mantle boundary. Another important difference between the two cases is that the temperature near the inner core boundary at the longitude of the heater is lower for global locking than for local locking, even though the thermal forcing in the global locking case is stronger. Lower temperature near the inner core boundary occurs with global locking because a large-scale cyclonic circulation develops near the heater, and this causes an intense upwelling to form beneath the heater lowering the temperature there. With local locking, the cyclonic circulation and upwelling are weaker.

[32] An example of the temperature measurement used to construct Figure 10 is shown in Figure 4. Figure 4 shows time series of temperature from four probes arrayed across the front. Probes A and B sample the cold region at the east side of the front, probe D samples the warm region at the west side of the front, and probe C straddles the front, and the large-amplitude temperature variations on this record correspond to the small fluctuations in the position of the front. These fluctuations are confirmation that the narrow front supports a large temperature difference. The temperature fluctuations recorded by probes on the warm side of the front have larger amplitude and higher frequency than on the cold side. This difference is an evidence for more convective heat transfer in the warm side compared to the cold side of the front, consistent with the inference we drew from dye mixing.

3.2.3. Statistical properties of the temperature time series

[33] A useful statistic is the standard deviation σ_T of temperature fluctuations, which is related to the magnitude of the convective heat flux (equation (16)). In the homogeneous boundary cases, σ_T is largest near the inner core boundary and in the equatorial plane [*Sumita and Olson*, 2000]. When heterogeneous heating is imposed, we find that σ_T near the core-mantle boundary is larger on the east side of the heater compared to the west side. This difference is consistent with the picture of warm plumes generated near the heater and advected eastward by the azimuthal flow.

[34] Temperature skewness, defined as $\Sigma(T - T_0)^3\sigma_T^{-3}/N$, is another useful diagnostic statistic. It measures deviations from symmetry of the fluctuations about T_0, the average temperature in the fluid. Nonzero values of this statistic occur near the thermal boundary layers [e.g., *Boubnov and Golitsyn*, 1990]. They also occur when there is some geometrically imposed asymmetry in the flow, such as results from sphericity.

[35] In experiments with homogeneous boundaries we find the skewness is negative at all locations. Evidently, this is because the basic temperature gradient decreases with radius; advection of this gradient results in the predominance of negative spikes of the temperature records. In contrast, with heterogeneous heat flux boundary conditions the temperature skewness is positive near the heater. We interpret this observation as indicating that these fluctuations are caused mostly by warm plumes originating at the heater.

[36] We have also computed the skewness of the time derivative of temperature. This particular statistic has been analyzed previously, for the case of thermal convection without rotation [*Belmonte and Libchaber*, 1996]. Time derivative skewness indicates a sawtooth pattern of temperature fluctuations. This statistic is positive when the saw teeth have steep increases and gentle decreases, and conversely, it is negative when the saw teeth lean the other way. We find that this statistic is negative at all regions of the fluid for convection with homogeneous boundary conditions. *Sumita and Olson* [2000] interpreted this as a result of westward drifting plumes having larger cyclonic vortices, an effect of Ekman pumping. In the present

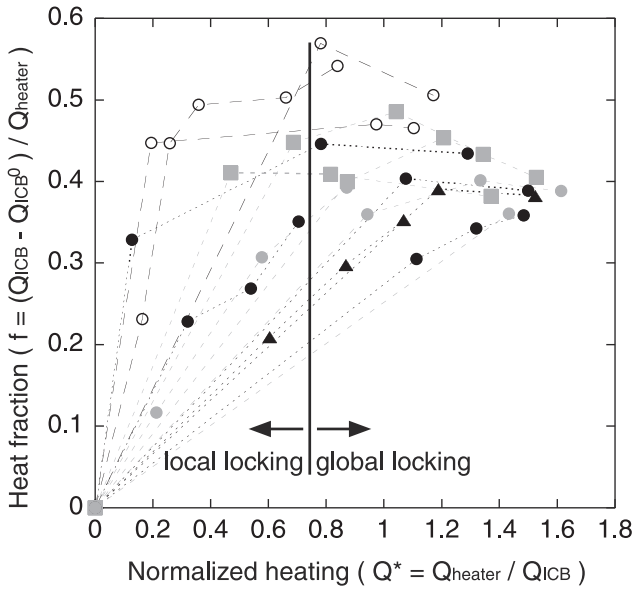

Figure 11. Relation between the fraction of heating transferred radially by convection, $f = (Q_{ICB} - Q_{ICB_0}/Q_{heater}$ versus the normalized heating $Q^* = Q_{heater}/Q_{ICB}$. Symbols indicate different Rayleigh number ranges: solid, $Ra/Ra_c = 24.7 \pm 0.7$; gray, $Ra/Ra_c = 27.7 \pm 0.7$; and open, $Ra/Ra_c = 42.1 \pm 1.6$. Circles, triangles, and squares correspond to a heater sizes of 10, 20, and 40° in longitude, respectively (latitudinal ranges are all 0–48°). Dashed lines join experiments from the same sequence of stepwise heating increase. A vertical line at $Q^* \sim 0.7$ is the boundary between the local and global locking regimes.

experiments we find that the time derivative skewness is positive in regions with eastward flow. For example, the data of Figure 4 have negative time derivative skewness at probes A and B, but a positive value at probe D, where the flow is eastward. Similarly, we interpret the positive values at probe D to indicate eastward drifting plumes with larger cyclonic vortices. This method of using skewness and the skewness of time derivative for inferring flow properties, such as direction of motion relative to a thermal gradient and asymmetry of vortices, may be useful in situations where flow visualization is difficult, such as in liquid metals.

3.2.4. Thickness of the thermal boundary layer

[37] With homogeneous thermal boundary conditions the radial temperature profile in the fluid is approximately hyperbolic, with its steepest gradient near the inner boundary. The temperature drop across the outer thermal boundary layer, ΔT_{TBL}, is negligible in this case compared to the total temperature difference across the shell ΔT [*Sumita and Olson*, 2000]. However, when the boundary heating is heterogeneous, these relationships change, since the thermal boundary layer beneath the heater develops an anomalously large temperature drop.

[38] For the situation shown in Figure 10 we can estimate the thickness of the thermal boundary layer beneath the heater δ_{TBL} as follows. First, the change in temperature across the copper hemispherical container is negligible. On the basis of the applied heat flow the radial temperature gradient within the copper hemisphere is estimated to be ~0.02°C. Therefore the surface probe measurement at the outer surface of the copper hemisphere gives a good estimate of the temperature at its inner surface. From Figure 10 we estimate a temperature drop of $\Delta T_{TBL}/\Delta T \sim 1$ across the thermal boundary layer (TBL). Assuming that all of the anomalous heat flux q_{heater} is conducted across the TBL, we obtain $\delta_{TBL} = k\Delta T_{TBL}/q_{heater} \sim 0.5$mm. This estimate indicates a very thin TBL, with a thickness the same order of magnitude as the Ekman boundary layer thickness $\delta_{Ek} = \sqrt{\frac{\nu}{2\Omega}} \sim 0.2$mm.

3.2.5. Heat flow measurements

[39] Figure 11 shows the relationship between the normalized heating Q^* and f, the fraction of anomalous boundary heating that is transported through the fluid across the spherical shell, for several sets of experiments. This fraction is defined by $f = (Q_{ICB} - Q_{ICB_0})/Q_{heater}$, where Q_{ICB} is the total heat flow at the inner core and the subscript zero indicates the case in the absence of heterogeneous heating. Results for different heater size and Rayleigh number are shown in Figure 11. From observation of convective pattern for each experiments, we infer a regime boundary at $Q^* \sim 0.7$. The location of this boundary does not appear to be sensitive to either the heater size or the Rayleigh number.

[41] Two features in Figure 11 deserve emphasis. First, it shows that f is approximately constant throughout the global locking regime. This value is $f \sim 0.4$ for $Ra/Ra_c \simeq 25$, which increases to $f \sim 0.5$ for $Ra/Ra_c \simeq 42$. Second, in the local locking regime, f approaches an asymptotic values faster for high Rayleigh numbers than for low Rayleigh numbers. We interpret this behavior as a consequence of larger efficiency of radial heat transfer (Nusselt number) at higher Rayleigh numbers. Assuming a $Nu \propto Ra^{1/2}$ relation [*Sumita and Olson*, 2000], the Nusselt number at $Ra/Ra_c \simeq 42$ is 1.3 times larger than at $Ra/Ra_c \simeq 25$, and scales well with the relative magnitude of the asymptotic values of f. We also conclude from Figure 11 that in terms of radial and lateral partitioning of anomalous heat, local locking is an intermediate regime between the convection with homogeneous thermal boundary conditions and the globally locked, boundary-driven flow.

3.3. A Summary of the Experiments

[42] We summarize our main findings from the experiments below.

1. A fully developed boundary-driven flow forms for $Q^* > 0.7$. In this regime the partitioning between the radial and lateral heat transfer becomes fixed.

2. Features of the boundary-driven flow under a sectorial heterogeneous heating spanning from low to high latitudes are a large-scale cyclonic circulation at the east of the heater, with a radially spiralling, stationary front along which a jet flows from the core-mantle boundary to the inner core boundary.

3. Effects of the geometry of heterogeneous heating are as follows: For high-latitude heating, there is a periodic formation and destruction of the front. For a zonal heating at low latitudes an eastward flow is generated, but a front does not form.

4. Statistics of temperature fluctuations have a close correlation with the direction and strength of fluid flows.

4. Fluid Dynamical Interpretation of the Experiments

4.1. Equation of Motion and Approximations

[43] The Boussinesq equation for fluid motion in a rotating frame is given by

$$\frac{\partial \boldsymbol{u}}{\partial t} + (\boldsymbol{u}\cdot\nabla)\boldsymbol{u} + 2\boldsymbol{\Omega}\times\boldsymbol{u} = -\frac{1}{\rho}\nabla P - \alpha \boldsymbol{g} T' + \nu\nabla^2\boldsymbol{u} \quad (2)$$

where $\boldsymbol{u}$ is the fluid velocity, $\boldsymbol{\Omega}$ is the rotation vector, ρ is the density, P is the pressure, α is the thermal expansion coefficient, $\boldsymbol{g}$ is acceleration of gravity, T' is the temperature perturbation, and ν is the kinematic viscosity.

[44] The primary force balance in the experiments can be determined from equation (2) using scaling arguments. For the case of a thermally homogeneous boundary, experiments at $Ek = 4.7 \times 10^{-6}$ and $Ra/Ra_c = 42$ yield radial fluid velocities of $V \sim 2.5 \times 10^{-3}$ m s^{-1} for the warm plumes. For these plumes the observed transverse width is $\delta \sim 4$ mm, and the measured temperature fluctuations are $T' \sim 0.3$ K in the vicinity of equatorial plane of the midshell [*Sumita and Olson*, 2000]. The magnitude of each term in equation (2) for these plumes is then (in units of m s^{-2}), $V^2/\delta \sim 2 \times 10^{-3}$, $2\Omega V \sim 8 \times 10^{-2}$, $\Delta P/\rho\delta \sim \alpha g T' D/\delta \sim 6 \times 10^{-2}$, $\alpha g T' \sim 2 \times 10^{-3}$, and $\nu(V/\delta^2) \sim 2 \times 10^{-4}$, respectively. Here the shell thickness ($D = 0.1$ m) is used for the pressure scale height. According to these estimates the primary force balance in the plumes is geostrophic, with advection and buoyancy terms forming a balance at the next order. Since the viscous term is generally small, it will be ignored in what follows.

[45] The corresponding vorticity equation is formed from the curl of equation (2):

$$\frac{\partial \boldsymbol{\omega}}{\partial t} + (\boldsymbol{u}\cdot\nabla)\boldsymbol{\omega} - (\boldsymbol{\omega} + 2\boldsymbol{\Omega})\cdot\nabla\boldsymbol{u} = \alpha\boldsymbol{g}\times\nabla T'. \quad (3)$$

We now derive approximate equations for the flow in cylindrical coordinates (r, ϕ, z), assuming quasi-geostrophy. We nondimensionalize these equations by taking the length scale D, and timescale D^2/ν and expand the velocity and vorticity in equation (3) in powers of a small parameter A, $\boldsymbol{u} = \boldsymbol{u}_0 + A\boldsymbol{u}_1$, $\boldsymbol{\omega} = \boldsymbol{\omega}_0 + A\boldsymbol{\omega}_1$. Then we collect like powers of A and Ekman number, Ek. Here we only summarize the results and rewrite them in dimensional form. The details of the derivation are described by *Cardin and Olson* [1994]. The lowest-order balance in equation (3) is

$$\frac{\partial \boldsymbol{u}_0}{\partial z} = 0, \quad (4)$$

which arises from $Ek \ll 1$. At the next order, equation (3) becomes

$$2\Omega\frac{\partial u_{r1}}{\partial z} = \frac{\alpha}{A}\left(g_z\frac{1}{r}\frac{\partial T'}{\partial \phi}\right), \quad (5)$$

$$2\Omega\frac{\partial u_{\phi 1}}{\partial z} = -\frac{\alpha}{A}(\boldsymbol{g}\times\nabla_{\mathrm{m}}T') = \frac{\alpha}{A}\left(g_r\frac{\partial T'}{\partial z} - g_z\frac{\partial T'}{\partial r}\right), \quad (6)$$

$$\frac{\partial \omega_{z0}}{\partial t} + (\boldsymbol{u}_0\cdot\nabla)\omega_{z0} - 2\Omega A\frac{\partial u_{z1}}{\partial z} = \alpha g_r\frac{1}{r}\frac{\partial T'}{\partial \phi}. \quad (7)$$

Here the centrifugal gravity is given by $g_r = r\Omega^2$, the laboratory gravity is given by g_z, and ∇_{m} denotes the gradient taken in the meridional plane.

4.2. Analysis of the Flow Pattern

4.2.1. Homogeneous boundary case

[46] Most of the dynamics in columnar flow are governed by equation (7), the axial vorticity equation. Here the important terms are vorticity advection and stretching terms on the left-hand side and the vorticity generation term on the right-hand side. To simplify the analysis of this equation, we first assume a steady state balance. The justification for (quasi) steady flow is the observation that the plumes drift very slowly in the experiment. In addition, we assume columnar flow, in which the velocity components parallel to the equatorial plane are invariant along the axial coordinate z. Following the procedure of *Busse* [1970] and extended to turbulent, columnar convection by *Cardin and Olson* [1994], we take a z average of equation (7). This is straightforward for all terms except the third term, which represents the vorticity change by column stretching in the rotating sphere. In averaging this term we need to consider the sphericity of the outer boundary. When we integrate this term in z from $z = 0$ to $z = L$, where L is the column height from the equator to the outer boundary, we obtain

$$\frac{1}{L}\int_0^L \frac{\partial u_{z1}}{\partial z}dz = \frac{1}{L}[u_{z1}]_0^L \simeq \frac{\eta(r)u_{r0}}{AL}. \quad (8)$$

In deriving this result we have used the relationship

$$u_{z1}(z = L) = \frac{\eta(r)}{A}u_{r0}(z = L), \quad (9)$$

where $\eta(r)$ is the slope at the outer boundary given by

$$\eta(r) = \frac{dL}{dr} = -\frac{r}{\sqrt{R^2 - r^2}}. \quad (10)$$

The steady state, inviscid, z-averaged vorticity equation then becomes

$$(\boldsymbol{u}_0\cdot\nabla_{\mathrm{e}})\omega_{z0} - 2\Omega\frac{\eta(r)}{L}u_{r0} = \alpha g_r\frac{1}{r}\frac{\partial \bar{T}}{\partial \phi}, \quad (11)$$

where ∇_{e} denotes the gradient in planes parallel to the equatorial plane and $\bar{T}$ is the column averaged temperature.

[47] Let us consider the axial fluid motion in a plume. From the slope effect a warm plume ($u_{r0} < 0$) is associated with a flow away from the equatorial plane. From continuity, there must be a convergence in the equatorial plane and vice versa for a cold plume. This difference explains why either warm or cold plumes are preferentially visualized by localized injection of dye. Warm plumes are preferentially visualized by dye released near the equatorial plane because the dye is drawn into them by the converging flow forming 2-D dye curtains. Conversely, it is hard to dye the cold plumes this way, since the flow diverges from the plume.

[48] A warm plume contains a temperature maximum at its center and is flanked by a cyclone and an eastward thermal gradient on its western side. On its eastern side a warm plume is flanked by an anticyclone and a westward thermal gradient. This structure would have bilateral symmetry about the plume axis, in the absence of rotation (i.e., second term of equation (11)). However, with rotation the

vortex stretching term generates additional cyclonic vorticity that destroys the bilateral plume symmetry. Vorticity balance can be achieved by enlarging the cyclonic vortices (smaller $|\partial T/\partial\phi|$ at the west of the warm plume compared to its east). This results in an asymmetric plume structure, and explains the skewness observed in the time derivative of temperature data as shown in section 3.2.2.

[49] Next we consider higher-order balances in the flow. Equation (6) describes the zonal flow with a shear in z, driven by the deviation of isotherms from isopotentials. Temperature measurements from experiments with a homogeneous boundary indicate that $\boldsymbol{g} \times \nabla_m T' < 0$. This term is mainly negative in the region near the equatorial plane, where a cold torus develops by the accumulation of cold plumes originating from the inner core boundary. Accordingly, equation (6) indicates that $\partial u_\phi/\partial z > 0$ over most of the hemisphere. Assuming that the zonal flow diminishes with distance from the equatorial plane, the positive shear indicates that the azimuthal flow is westward near the equatorial plane ($u_\phi < 0$) contributing to the westward flow we observe in the experiments.

4.2.2. Heterogeneous boundary case

[50] Primary force balance of the plumes under a thermally heterogeneous boundary remains quasi-geostrophic, and equation (11) can be used to understand the flow pattern. Dropping off the advection term, it shows that a negative vorticity generation by an eastward decrease of temperature ($\partial\bar{T}/\partial\phi < 0$) is cancelled by a positive vorticity generation from downwelling which causes vortex stretching. This explains the eastward phase shift of the downwelling region relative to the heater. A downwelling jet forms where the warm eastward flow and cold westward flow converge.

[51] The higher-order zonal flow given by equation (6) is driven by latitudinal temperature variation. For a sectorial heating case this effect is estimated to be small because the zonal flow which feeds into the geostrophic jet should also be columnar. On the other hand, for a zonal heating case this flow becomes relatively important. In this case, a complete reversal of the direction of the zonal flow resulted for $\partial T'/\partial z < 0$, which results in $\partial u_\phi/\partial z < 0$. Assuming that the magnitude of u_ϕ decreases with distance from the equatorial plane, we find that the zonal flow becomes eastward ($u_\phi > 0$). This suggests that the latitudinal temperature variation is the cause for the eastward flow for this case.

4.3. Scaling Relations

4.3.1. Homogeneous temperature boundary case

[52] Scaling relationships for the important variables in the flow can be obtained using equation (11). First, we determine how the variables describing the thermal plumes scale with the external parameters. Similar scaling relation for thermal plumes in the homogeneously heated case have previously been obtained by *Cardin and Olson* [1994] and *Aubert et al.* [2001]. Two independent relations between plume variables are obtained by assuming a balance between the absolute value of the all three terms in (11). Assuming $\omega_{z0} \sim V/\delta$, we find

$$\frac{V^2}{\delta^2} \sim 2\Omega\frac{\eta}{L}V \sim \frac{\alpha g_r T'}{\delta}. \tag{12}$$

Table 2. Comparison of Experiments and Model Results

Parameter	Experiments	Model	Units
δ (equation (14))	2×10^{-3}[a]	2×10^{-3}	m
V (equation (15))	1×10^{-3}[a]	2×10^{-3}	m s^{-1}
T' (equation (16))	0.3[a]	0.1	K
V_{TW} (equation (19))	1.5×10^{-3}[b]	1.1×10^{-3}	m s^{-1}
ΔT_{CMB} (equation (20))	$\simeq$7.6[b]	3.3	K
δ_{jet} (equation (22))	5×10^{-3}[b]	3×10^{-3}	m
V_{jet} (equation (23))	5×10^{-3}[b]	7×10^{-3}	m s^{-1}
d (equation (25))	0.15[b]	0.16	m

[a] At midshell for a thermally homogeneous case ($\Delta T = 11°C$, $Ra/Ra_c = 42$).
[b] For the case shown in Figure 2c, $\Delta T_{front} \sim 1.5$ K at 8.1 cm from inner core boundary.

A third relationship comes from the relationship between temperature fluctuations T' and convective heat transfer q in the fluid:

$$T' = \frac{q}{\rho C_p V}. \tag{13}$$

Combining the above equations we obtain the following scaling laws for δ, V and T':

$$\delta \sim \left[(\alpha g_r)\left(\frac{q}{\rho C_p}\right)\left(\frac{L}{2\Omega\eta}\right)^3\right]^{1/5}, \tag{14}$$

$$V \sim \left[(\alpha g_r)^2\left(\frac{q}{\rho C_p}\right)^2\left(\frac{L}{2\Omega\eta}\right)\right]^{1/5}, \tag{15}$$

$$T' \sim \left[(\alpha g_r)^{-2}\left(\frac{q}{\rho C_p}\right)^3\left(\frac{L}{2\Omega\eta}\right)^{-1}\right]^{1/5}. \tag{16}$$

There is an implied radial dependence in these scalings because g_r, q, L/η all depend on radius. However, we propose that we can specify a certain radius to evaluate the slope factor $L/\eta = (R^2 - r^2)/r$ (R is the core-mantle boundary radius). We infer this because the slope factor determines the wave number of the plumes and the experiments show that this does not change with radius in the regime of geostrophic turbulence. According to the thin shell model of *Tilgner and Busse* [1997] the observed wave number of $m \simeq 108$ at this Ekman number corresponds to the slope at the latitude of 31° at $r = 0.13$ m. Therefore we use the slope at this location in our analysis.

[53] A good agreement of this scaling with experimental measurements was already demonstrated by *Cardin and Olson* [1994] and *Aubert et al.* [2001], and similarly, we compare our measurements below. We evaluate q by $q = Q_{ICB}/2\pi r R_{ICB}$, where Q_{ICB} is the total heat flow at the inner core boundary. We assume Q_{ICB} is convective heat transfer, that is, heat conduction can be neglected. This is validated from the fact that the temperature within the fluid is nearly isothermal except near the inner core boundary [*Sumita and Olson*, 2000]. A comparison of the values obtained from experiments and those estimated from scaling relations are given in Table 2, showing a fair agreement. Among these scales, T' can be determined with best ease and precision in our apparatus. In Figure 12 we

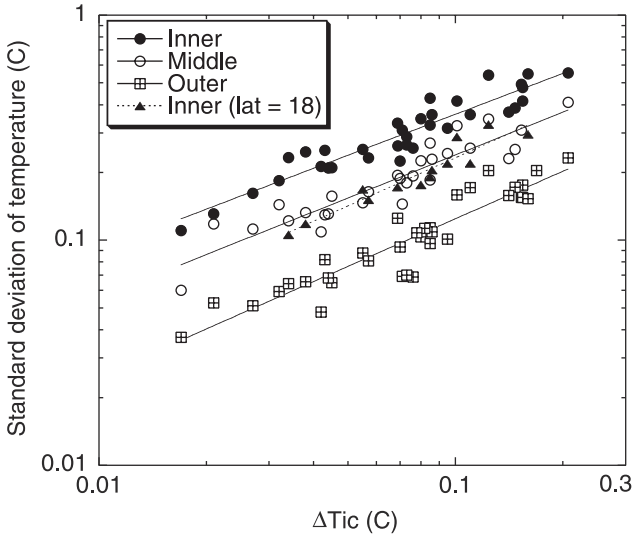

Figure 12. Relationship between the standard deviation of temperature fluctuations in the fluid (T') and temperature increase measured in the inner core cooling system ($\Delta T_{IC} \propto$ heat flux at inner core boundary) for cases with thermally homogeneous boundary conditions. Lines indicate power law fits given by inner, (r = 3.1 cm) $T' = 1.45\Delta T_{IC}{}^{0.60}$; middle, ($r$ = 5.6 cm) $T' = 1.02\Delta T_{IC}{}^{0.63}$; outer, ($r$ = 8.1 cm) $T' = 0.62\Delta T_{IC}{}^{0.70}$; inner, (latitude of 18) (r = 3.1 cm) $T' = 1.19\Delta T_{IC}{}^{0.71}$. (Note that T', ΔT_{IC} are nondimensionalized by 1 K. Each probe is located r cm from the inner core boundary. The inner (latitude of 18) probe is located at latitude 18°; the others are in the equatorial plane.)

plot the standard deviation of the temperature fluctuations in the fully developed turbulence (the dual convective regime of *Sumita and Olson* [2000]) as a function of the temperature rise of the circulating water in the inner core, which is proportional to the total heat flux at the inner core boundary. The scaling law given in equation (16) predicts $T' \propto q^{0.6}$, which agrees well with measurements near the inner core boundary. The scaling predicts a relation $T' = 0.34\Delta T_{IC}^{0.6}$ for the inner probe. This coefficient is smaller than the measured value at the equatorial plane by a factor of 4, indicating that the heat transfer is larger near the equatorial plane as compared to the column averaged heat transfer.

4.3.2. Heterogeneous boundary case

[54] We consider the case of a heated patch with a latitude dimension H_θ and a longitude dimension H_ϕ. The eastward equatorial thermal wind flow V_{TW} can be estimated using equation (7). Here we neglect the inertial terms which are unimportant in the eastward flow and obtain

$$V_{TW} \sim \frac{\alpha g_r \Delta T_{CMB}}{2\Omega}, \tag{17}$$

where ΔT_{CMB} is the longitudinal temperature variation of the fluid beneath the thermal boundary layer at core-mantle boundary. The convective heat flux advected by this flow is

$$q_{TW} = \rho C_p \Delta T_{CMB} V_{TW}. \tag{18}$$

From equations (17) and (18) we obtain

$$V_{TW} \sim \left(\frac{\alpha g}{2\Omega\rho C_p} q_{TW}\right)^{1/2}, \tag{19}$$

$$\Delta T_{CMB} \sim \left(\frac{2\Omega}{\alpha g \rho C_p} q_{TW}\right)^{1/2}. \tag{20}$$

In general, the cross section area of the zonal flow and the size of the heater are different, so q_{TW} is different from q_{heater}. We can relate these two quantities as follows.

$$q_{TW} \sim \epsilon\left(\frac{S}{dH_\theta}\right) q_{heater} = \epsilon\left(\frac{H_\phi}{d}\right) q_{heater}, \tag{21}$$

where $S = H_\theta \times H_\phi$ is the heater area, d is the depth scale of the eastward flow, and ϵ is the fraction of the anomalous boundary heat flux advected eastward from the heater. We estimate it to be nearly one because of the predominantly eastward flow near the heater. For the case in Figure 2c, H_ϕ = 0.025 m and $d \simeq$ 0.015 m, so $H_\phi/d \simeq 1.7$. Assuming $\epsilon = 1$, we evaluate V_{TW} and ΔT_{CMB} (Table 2) and find that there is a fair agreement between the experiment and the model. We note that measured ΔT_{CMB} is the temperature variation on the outer surface of the hemisphere, and the actual ΔT_{CMB} in the fluid beneath the thermal boundary layer should be smaller than this.

[55] Next, we derive scaling relations for the front and jet. We rewrite equations (14) and (15) in terms of the temperature difference across the front ΔT_{front}, instead of convective heat flux. This gives

$$\delta_{jet} \sim (\alpha g \Delta T_{front})^{1/3} \left(\frac{L}{2\Omega\eta}\right)^{2/3}, \tag{22}$$

$$V_{jet} \sim (\alpha g \Delta T_{front})^{2/3} \left(\frac{L}{2\Omega\eta}\right)^{1/3}. \tag{23}$$

A similar comparison is given in Table 2, which also shows an agreement within a factor 2.

[56] The zonal flow V_{TW} and the radial jet V_{jet} scaled above are related in the following way. Because the dye advected by eastward flow feeds into the 2-D jet, we obtain from the continuity equation the following relationship between fluid velocity in the thermal wind and the jet:

$$V_{TW} d \sim V_{jet} \delta_{jet}. \tag{24}$$

This relationship should apply at the junction of eastward flow and the jet. Using the measured values from this region, we find left-hand side $\simeq 2.3 \times 10^{-5}$ and right-hand side $\simeq 2.5 \times 10^{-5}$ m^2 s^{-1}, confirming this assumption.

[57] The temperature difference across the front can be regarded as the typical lateral temperature variation in the fluid responsible for the boundary-driven flow. Thus $\Delta T_{front} \sim \Delta T_{CMB}$. For the case shown in Figure 10 it is ~0.25 (nondimensional). With this relation, we substitute equations (19), (20), (22), and (23) into equation (24) and obtain $d \simeq L/\eta = (R^2 - r^2)/r$. This is a geometrical relation equivalent to $R - r = d/2$ and $d/R \ll 1$. It corresponds to

a situation where the eastward flow feeds into the jet at a depth centered around $d/2$, consistent with what we observe.

[58] The depth scale of the eastward flow d is assumed to be comparable to the thermal diffusion length scale using eddy diffusivity κ_{eddy}:

$$d \sim \left(L_\phi \kappa_{eddy}/V_{TW}\right)^{1/2}. \quad (25)$$

We evaluate for the situation of Figure 2c by taking $L_\phi \sim 0.1$ m as the lateral length scale of the eastward flow, $\kappa_{eddy} \sim \delta V \sim 4 \times 10^{-6}$ m^2 s^{-1} (δ, V are for the plumes: $\delta \simeq 4$ mm, $V \sim 10^{-3}$ m s^{-1}) and $V_{TW} \sim 1.5 \times 10^{-3}$ m s^{-1}. Comparison between experiments and model (Table 2) shows a good agreement.

[59] Because both κ_{eddy} and V_{TW} increase with q_{heater}, this scaling leads to $d \propto q_{heater}^{1/15}$, showing that d is only weakly dependent on q_{heater}, consistent with the experimental results. It then follows that when H_θ is fixed, as in the situation of Figure 7, from equation (21) we have an approximate relation $q_{TW} \propto Sq_{heater}$. This shows that effective heat flux advected by the eastward flow depends on the total heating Sq_{heater}, as observed in Figure 7.

[60] The jet was observed to decelerate as it nears the inner core boundary. There are two possible explanations for this. One is the smaller available buoyancy nearer the inner core boundary because of smaller gravity. The other is the larger axial length scale of the front as it nears the inner core boundary, which reduces the fluid velocity there.

4.4. Explanation for Front Formation

[61] Our experiments suggest that there are two basic conditions for front formation. The first condition is the geometry of the heterogeneity. Following our argument in section 4.3.2, a flow pattern which forms a convergence is needed. Not all heater geometries produce this result. For example, the case with zonal, equatorial heating does not produce a front because it does not lead to convergent flows. The second condition is the need for a sufficient heating at the heater. We expect that if the heterogeneous thermal forcing at the core-mantle boundary overwhelms that of the mean convection, then a front can be sustained by the boundary-driven flow. The empirical law for front formation,

$$Q^* > \frac{Q_{heater}}{Q_{ICB}} \simeq 0.7 \sim 1, \quad (26)$$

can be restated as follows: Q_{ICB} is the total radial heat transfer between the core-mantle boundary and inner core boundary, and we can separate it into the radial heat transfer in the active and quiet regions as defined in section 3.2.2

$$Q_{ICB} = Q_{active} + Q_{quiet}. \quad (27)$$

When a front forms, most of the heat transferred in the active region originates from the heater

$$Q_{active} \simeq f\ Q_{heater}, \quad (28)$$

where f is the fraction of heat imposed by the heater which is transferred radially (section 3.2.5). Substituting equations (27) and (28) into equation (26), we have

$$\left(\frac{1}{f} - 1\right)\frac{Q_{active}}{Q_{quiet}} \simeq 1. \quad (29)$$

With experimental values of $f \simeq 0.5 \pm 1$ we find that a front forms at a threshold of $Q_{active} \sim Q_{quiet}$. This implies that fronts form when the radial heat transfer by the boundary-driven flow constitutes the major part of the total heat flow.

[62] The formation of a large-scale cyclonic circulation can alternatively be interpreted in terms of preferred pattern for heat transfer. Under a homogeneous boundary, warm plumes cannot traverse across the shell and mix with the ambient fluid at midshell. The formation of a radially extending front can be viewed as an efficient way to transfer the anomalous boundary heating. Such coexistence of two different length scales, the narrow plumes and broad large-scale circulation, has also been observed in nonrotating thermal convection experiments at high Rayleigh numbers (reviewed by *Siggia* [1994]). In this regime, plumes do not traverse across the vertical depth scale, and instead a large-scale flow forms which advects the plumes laterally.

[63] The formation of the front provides a way to estimate the eddy thermal diffusivity in the experiments. Because the front is stationary, the following thermal balance should hold across the shell:

$$v_r \frac{\partial T}{\partial r} \sim \kappa_{eddy} \frac{1}{r^2} \frac{\partial^2 T}{\partial \phi^2}. \quad (30)$$

This leads to the following estimate of eddy diffusivity:

$$\kappa_{eddy} \sim \left(\frac{\Delta T}{\Delta T_{front}}\right)\left(\frac{V_{jet}\delta_{jet}^2}{\Delta R}\right), \quad (31)$$

where ΔT is the temperature difference across the shell near the jet and the length scale of the front was taken to be the shell thickness ΔR. For the situation in Figure 2c the measurements are $\Delta T \sim 7$ K, $\Delta T_{front} \sim 2$ K, $V_{jet} \sim 5 \times 10^{-3}$ m s^{-1}, and $\delta_{jet} \sim 4$ mm, and we obtain $\kappa_{eddy} \sim 3 \times 10^{-6}$ m^2 s^{-1}. This agrees with our estimate used in evaluating equation (25).

5. Comparison With Numerical Calculations

[64] First, we compare cases in which the boundary heating is a function of longitudinal. Most numerical calculations have focused on this type of heterogeneous convection.

[65] The most obvious similarity between our experiments and calculations with azimuthally variable heating is the eastward phase shift of the downwelling, relative to the high boundary heat flux region. This has been reported by the nonmagnetic convection calculations (case A described in section 1). A deeper penetration of the boundary driven flow with heating is also a common feature and was reported by *Sun et al.* [1994]. On the other hand, there are some significant differences between our experiments and these calculations. The fine-scaled features such as the plumes and jets are not well reproduced in the calculations.

Also, the eastward phase shift in the calculations is less than we observe.

[66] These differences may be due in part to the difference in parameter values, but they may also be due to limited spatial resolution in the numerical calculations. The experiments were done at a Rayleigh number of the order of 10^8. At such large Rayleigh numbers, heat advection is dominant in the fluid away from thin boundary layers, as evidenced by the large Péclet number, $Pe = VL/\kappa \sim 700$ (here we assume $V \sim 10^{-3}$ m s^{-1}, and $L = 0.1$ m). For comparison, numerical calculations are typically made at much lower Rayleigh numbers $\leq 10^7$ and correspondingly smaller Péclet numbers. This difference tends to reduce the role of fronts and jets in the calculations, compared with our experiments. We note, however, that a similar large-scale spiral with a temperature front was obtained from a magnetoconvection calculation under a homogeneous heat flux boundary [*Olson and Glatzmaier*, 1996]. The spiral in their calculation seem to result from minimizing the distortion of the toroidal field, yet transferring heat radially. Another significant difference is the geometry of the boundary heating, particularly its azimuthal wave number. Most of our experiments were made with a single heater, i.e., degree 1 heterogeneity. This contrasts with numerical calculations which assume a larger wave number boundary heating pattern, typically spherical harmonic degree two or higher. The lower the azimuthal heating wave number, the larger the eastward phase shift, which accounts for the larger phase shift observed in the experiments, compared to the calculations.

[67] Next, we compare our results to calculations with a latitudinal variation of boundary heat flow. *Hart et al.* [1986a, 1986b] made a study of a convection driven by latitudinal boundary heat flow variations, combining both their space lab experiments and numerical simulations. In the space lab experiments the gravity vector was directed radially inward and the outer boundary in the polar region was maintained at a higher temperature than the equatorial region. Qualitatively, this arrangement is similar to our experiments with a banded heating around the equator (section 3.1.6). Their calculations were made at $Ek = 6 \times 10^{-2}$, and they found a downwelling near the equator, accompanied by an eastward flow, a result they interpret in terms of angular momentum transfer. Although the Ekman number in their study was larger than ours, the flow features they found are qualitatively similar to those described in section 3.1.6, indicating a common cause for the eastward flow in the two experiments.

6. Applications to the Earth's Core

6.1. Is Global Locking Possible in the Core?

[68] In order to determine if the globally locked flow that we observe is possible in the core, we must estimate the boundary heterogeneity index Q_{active}, Q_{quiet} in the core. First, we estimate the lateral variation of heat flux at core-mantle boundary. The temperature of the outer core at the core-mantle boundary is estimated to be about 4000 ± 200 K [*Boehler*, 2000]. The shear wave velocity at the base of the mantle (i.e., a vertical average of lower few hundred km) by *Castle et al.* [2000] varies laterally by about +2% to −5%. *Castle et al.* [2000] estimate that this variation corresponds to a lateral temperature variation of ∼1500 K. The lower mantle geotherm of *Boehler* [2000] gives a lower mantle temperature above the thermal boundary layer (∼150 km above core-mantle boundary) near ∼2800 K. Assuming a lateral temperature variation of ±500 K at this depth, we find that the heat flux at the core-mantle boundary, q_{CMB}, can vary about a factor of 2.

[69] Next, we estimate the size of the highest heat flow region. A prominent, seismically fast region near the core-mantle boundary beneath east Asia is a common feature in seismic tomography models derived both from compressional and from shear waves [reviewed in *Garnero*, 2000]. We assume, as others have, that this region represents cold mantle, below which the core-mantle boundary heat flow is high. (Recall that warm, high boundary heat flow region in the experiments correspond to cold, high boundary heat flow region in the core, because of the direction of gravity is reversed in the experiments). Using the seismic tomography model by *van der Hilst and Kárason* [1999], we assume that this region covers ∼10% of the total core-mantle boundary surface area.

[70] The total heat flow at the core-mantle boundary is estimated to be about $Q_{\text{CMB}} \simeq 3 \times 10^{12}$ W ($q_{\text{CMB}} \simeq 20$ mW m^{-2}) (reviewed by *Sumita and Yoshida* [2002]) of which $\sim 2.7 \times 10^{12}$ W ($q_{\text{ad}} \simeq 18$ mW m^{-2}) is the heat conducted down the core adiabat. As a result, convective contribution to heat flux in the core below the core-mantle boundary is $\sim 3 \times 10^{11}$ W ($q_{\text{conv}} \simeq 2$ mW m^{-2}).

[71] *Sumita and Olson* [1999] have proposed a method for estimating the magnitude of the lateral variations in the convective heat transfer in the core in terms of other parameters. Following the estimates made above, as an example assume that the patch with high heat flow covering 10% of core-mantle boundary beneath east Asia has twice the heat flux of the surrounding regions. With a conductive heat flow of $q_{\text{ad}} \simeq 18$ mW m^{-2} estimated above, the total (convective) heat flow in this region becomes 2.7×10^{11} W. On the basis of experimental results we assume that ∼50% of this total is transferred radially downward into the core (and the remaining 50% is transferred laterally). We then obtain $Q_{\text{active}} \simeq 1.4 \times 10^{11}$ W and $Q_{\text{quiet}} \simeq 1.6 \times 10^{11}$ W. The fraction of heat that is transferred radially downward into the core is probably higher than the experimental value of $f \simeq 0.5 \pm 0.1$, because the copper hemisphere in the experiment permits more lateral heat conduction than does the lower mantle. Allowing for this difference, Q_{active} would be larger and Q_{quiet} would be smaller than the estimate above.

[72] The parameters of this calculation, such as the area and amplitude of the high heat flux anomaly are quite uncertain and may vary depending on which tomographic models are used. Even so, this estimate does suggest that Q_{active} can be comparable to Q_{quiet}. The regime of global locking is plausible in the core.

6.2. Spatial and Temporal Scales of Flow

[73] We now estimate the scales of boundary-driven flow in the core. First, we estimate the eddy diffusivity in the core as $\kappa_{\text{eddy}} \sim \delta V \sim 0.5$ m^2 s^{-1}. Here, $\delta \sim 1.5$ km, $V \sim 3 \times 10^{-4}$ m s^{-1} were obtained using equations (14) and (15) with $q \sim 2$ mW m^{-2} (η is evaluated at latitude of 31°).

[74] We can estimate the mixing timescale in the core using the eddy diffusivity as $D^2/\kappa_{\text{eddy}} \sim O(10^5)$ years. This

indicates that the boundary-driven flow can develop quickly as compared to the timescale of the change in the boundary thermal forcing, which is estimated by the mantle overturn time of $\sim O(10^8)$ years.

[75] We consider the flow scales in a global locking regime. For the eastward thermal wind its depth extent d can be similarly estimated from equation (25) as

$$d \sim 90\left(\frac{L_\phi}{3600\ \text{km}}\right)^{1/2}\left(\frac{2\times 10^{-4}\text{m s}^{-1}}{V_{\text{TW}}}\right)^{1/2}\text{km}. \quad (32)$$

Its flow velocity and temperature scales are evaluated using equations (19), (20), and (21). Using $q_{\text{heater}} = 18$ mW m^{-2}, $\alpha = 10^{-5}$ K^{-1}, $\Omega = 7.3 \times 10^{-5}$ s^{-1}, $\rho = 1.2 \times 10^4$ kg m^{-3}, $C_p = 700$ J K^{-1} kg^{-1}, $g = 10$ m s^{-2}, $\epsilon = 1$, $H_\phi = 3600$ km, we obtain

$$V_{\text{TW}} \sim 2\times 10^{-4}\left(\frac{q_{\text{TW}}}{0.7\ \text{W m}^{-2}}\right)^{1/2}\text{m s}^{-1}, \quad (33)$$

$$\Delta T_{\text{CMB}} \sim 4\times 10^{-4}\left(\frac{q_{\text{TW}}}{0.7\ \text{W m}^{-2}}\right)^{1/2}\text{K}. \quad (34)$$

As is the case in the experiments, we assume that the eastward flow feeds into the jet (equation (24)) and that the temperature difference across the front is comparable to the lateral temperature difference which drives the eastward flow ($\Delta T_{\text{front}} \sim \Delta T_{\text{CMB}}$). Similarly, it follows that $L/\eta = d$, and using equations (22) and (23), we can obtain the estimates for the width and velocity of the jet along the front as

$$\delta_{\text{jet}} \sim 2\left(\frac{\Delta T_{\text{front}}}{4\times 10^{-4}\text{K}}\right)^{1/3}\text{km}, \quad (35)$$

$$V_{\text{jet}} \sim 9\times 10^{-3}\left(\frac{\Delta T_{\text{front}}}{4\times 10^{-4}\ \text{K}}\right)^{2/3}\text{m s}^{-1}. \quad (36)$$

Comparing the above scales, we find that the width and velocity of the eastward thermal wind and the jet differ by more than an order of magnitude.

6.3. Hemispherical Variation of Core Structure

[76] *Sumita and Olson* [1999] interpreted the pattern of flow in the core inferred from geomagnetic secular variation in terms of the experimentally observed flow pattern in the globally locked regime. In Figure 3 this interpretation is indicated, based upon the assumption that the seismically fast region in the lower mantle beneath east Asia corresponds to the highest heat flow patch on the core-mantle boundary. The azimuthal flow pattern in the experiment is kinematically similar to the pattern inferred from geomagnetic secular variation. They also pointed out that the inferred high heat flow region near the inner core boundary at the west of the front coincides with the region of large inner core seismic anisotropy. In this section, we elaborate on the comparison between the experimental results and inferred flow patterns in the Earth's core.

[77] A hemispherical variation of azimuthal flow near the equator of the core-mantle boundary, with a westward flow in the Atlantic hemisphere and a generally eastward flow in the Pacific hemisphere, is common to most core flow models [reviewed in *Bloxham and Jackson*, 1991], independent of the assumptions used to derive the flow model. The longitude where the azimuthal flow turns from west to east approximately corresponds to the central longitude of the high heat flux patch in the experiments. On the core-mantle boundary, it roughly corresponds to the longitude of the center of the high seismic velocity region in the lower mantle beneath east Asia. In terms of azimuthal flow, the experimental results for globally locked convection are compatible with the structure of the core and mantle in this region.

[78] The experiments also predict a broad upwelling region just west of the high core-mantle boundary heat flux patch, and a narrow downwelling to the east, where the jet forms. Core flow models based on geomagnetic secular variation show a variety of upwelling patterns, depending on model assumptions. The core flow model that agrees best with the experimental upwelling and downwelling pattern is tangential geostrophy. Core flows based on tangential geostrophy show strong, linear upwellings located west of the east Asia seismic velocity high, approximately at the longitude of India [*Bloxham and Jackson*, 1991; *Bloxham*, 1992], in agreement with the experimental pattern. We speculate that this agreement may be due to similar constraints on the flow in each case. Tangential geostrophy constrains upwellings to occur where the meridional flow is toward the equator. This particular relationship between meridional and radial velocity components is qualitatively the same as in the columnar flow seen in our experiments.

[79] Our experiments show that the longitude phase shift between the terminus of the front at inner core boundary and its origin on the core-mantle boundary (in Figure 3 this is $\sim 180°$), is an increasing function of $Q_{\text{active}}/Q_{\text{quiet}}$. In principle, the origin on core-mantle boundary can be constrained from the hemispherical outer core flow pattern and the inner core boundary terminus from the hemispherical variation of the inner core seismic structure [*Sumita and Olson*, 1999]. In the core the presence of the magnetic field is likely to reduce the phase shift [*Yoshida and Hamano*, 1993]. The phase shift angle in the core is a function of $Q_{\text{active}}/Q_{\text{quiet}}$ and magnetic field strength and may be used to constrain these unknowns.

[80] Previous estimates on lateral variation of temperature beneath core-mantle boundary suggest that the temperature difference across the front is very small and seismically undetectable [*Stevenson*, 1987; *Bloxham and Jackson*, 1990]. However, *Tanaka and Hamaguchi* [1993] reported a hemispherical heterogeneity in the outer core with a pattern consistent with the model of *Sumita and Olson* [1999]. Our experiments also suggest that the light elements released from inner core solidification would preferentially accumulate beneath the warm region wedged between the core-mantle boundary and the front (region II in Figure 3). In the model of *Sumita and Olson* [1999] this corresponds to the region beneath the Pacific. Such lateral variation of composition beneath the core-mantle boundary can contribute to the lateral variation of seismic velocity at the top of the outer core and may even allow shear waves to propagate. In light of these possibilities, the existence of possible

lateral heterogeneity in the outer core deserves further examination.

[81] Finally, we point out some similarities between the flow structure in these experiments and other geophysical fluids. The jet we observe in the globally locked regime has kinematical and dynamical similarities to the western boundary currents in the ocean, such as the Gulf Stream in the Atlantic. As with the Gulf Stream, the experimental jet is a quasi-geostrophic current driven by a combination of buoyancy forces and the large-scale pressure difference between two adjacent masses of fluids at different temperatures. Instabilities of the jet develop, reminiscent of Gulf Stream eddies and rings. There is a further similarity in the direct convective heat transport by the jet from the outer to the inner boundary of the spherical shell, like the Gulf Stream transports heat to high latitudes across the Atlantic. We speculate that a structure like the Gulf Stream might exist in the outer core, driven by large scale pressure difference caused by the thermally heterogeneous forcing of the lower mantle. Such a dynamical structure would result in a longitudinally heterogeneous "climate" in the core and exert control on the long-term asymmetry of the geomagnetic field and on the pattern of inner core solidification.

[82] **Acknowledgments.** We thank J. Aubert for sending a preprint, and G. Glatzmaier and J. Whitehead for helpful comments on the manuscript. I.S. was supported by JSPS Postdoctoral Fellowships for Research Abroad at Johns Hopkins University. Experiments were supported by the Geophysics Program of NSF.

References

Aubert, J., D. Brito, H.-C. Nataf, P. Cardin, and J.-P. Masson, A systematic experimental study of rapidly rotating spherical convection in water and liquid gallium, *Phys. Earth Planet. Inter.*, *128*, 51–74, 2001.

Belmonte, A., and A. Libchaber, Thermal signature of plumes in turbulent convection: The skewness of the derivative, *Phys. Rev. E*, *53*, 4893–4898, 1996.

Bergman, M. I., Measurements of elastic anisotropy due to solidification texturing and the implications for the Earth's inner core, *Nature*, *390*, 60–63, 1997.

Bergman, M. I., L. Giersch, M. Hinczewski, and V. Izzo, Elastic and attenuation anisotropy in directionally solidified (hcp) zinc, and the seismic anisotropy in the Earth's inner core, *Phys. Earth Planet. Inter.*, *117*, 139–151, 2000.

Bloxham, J., The steady part of the secular variation of the Earth's magnetic field, *J. Geophys. Res.*, *97*, 19,565–19,579, 1992.

Bloxham, J., The effect of thermal core-mantle interactions on the paleomagnetic secular variation, *Philos. Trans. R. Soc. London, Ser. A*, *358*, 1171–1179, 2000a.

Bloxham, J., Sensitivity of the geomagnetic axial dipole to thermal core-mantle interactions, *Nature*, *405*, 63–65, 2000b.

Bloxham, J., and D. Gubbins, Thermal core-mantle interactions, *Nature*, *325*, 511–513, 1987.

Bloxham, J., and A. Jackson, Lateral temperature variations at the core-mantle boundary deduced from the magnetic field, *Geophys. Res. Lett.*, *17*, 1997–2000, 1990.

Bloxham, J., and A. Jackson, Fluid flow near the surface of the Earth's outer core, *Rev. Geophys.*, *29*, 97–120, 1991.

Bloxham, J., D. Gubbins, and A. Jackson, Geomagnetic Secular Variation, *Philos. Trans. R. Soc. London, Ser. A*, *329*, 415–502, 1989.

Boehler, R., High-pressure experiments and the phase diagram of lower mantle and core materials, *Rev. Geophys.*, *38*, 221–245, 2000.

Boubnov, B. M., and G. S. Golitsyn, Temperature and velocity field regimes of convective motions in a rotating plane fluid layer, *J. Fluid Mech.*, *219*, 215–239, 1990.

Buffett, B. A., Earth's core and the geodynamo, *Science*, *288*, 2007–2012, 2000.

Busse, F. H., Thermal instabilities in rapidly rotating systems, *J. Fluid Mech.*, *44*, 441–460, 1970.

Busse, F. H., and C. R. Carrigan, Laboratory simulation of thermal convection in rotating planets and stars, *Science*, *191*, 81–83, 1976.

Cardin, P., and P. Olson, Chaotic thermal convection in a rapidly rotating spherical shell: consequences for flow in the outer core, *Phys. Earth Planet. Inter.*, *82*, 235–259, 1994.

Castle, J. C., K. C. Creager, J. P. Winchester, and R. D. van der Hilst, Shear wave speeds at the base of the mantle, *J. Geophys. Res.*, *105*, 21,543–21,557, 2000.

Creager, K. C., Large-scale variations in inner core anisotropy, *J. Geophys. Res.*, *104*, 23,127–23,139, 1999.

Creager, K. C., Inner core anisotropy and rotation, in *Earth's Deep Interior: Mineral Physics and Tomography From the Atomic to the Global Scale, Geophys. Monogr. Ser.*, vol. 117, edited by S. Karatoet al., pp. 89–114, AGU, Washington, D.C., 2000.

Garcia, R., and A. Souriau, Inner core anisotropy and heterogeneity level, *Geophys. Res. Lett.*, *19*, 3121–3124, 2000.

Garcia, R., and A. Souriau, Correction to "Inner core anisotropy and heterogeneity level" by Raphaël Garcia, and Annie Souriau, *Geophys. Res. Lett.*, *28*, 85–86, 2001.

Garnero, E. J., Heterogeneity of the lowermost mantle, *Annu. Rev. Earth Planet. Sci.*, *28*, 509–537, 2000.

Gibbons, S. J., and D. Gubbins, Convection in the Earth's core driven by lateral variations in the core-mantle boundary heat flux, *Geophys. J. Int.*, *142*, 631–642, 2000.

Glatzmaier, G. A., and P. H. Roberts, Simulating the geodynamo, *Contemp. Phys.*, *38*, 269–288, 1997.

Glatzmaier, G. A., R. C. Coe, L. Hongre, and P. H. Roberts, The role of the Earth's mantle in controlling the frequency of geomagnetic reversals, *Nature*, *401*, 885–890, 1999.

Hart, J. E., J. Toomre, A. E. Deane, N. E. Hurlburt, G. A. Glatzmaier, G. H. Fichtl, F. Leslie, W. W. Fowlis, and P. A. Gilman, Laboratory experiments on planetary and stellar convection performed on Spacelab 3, *Science*, *234*, 61–64, 1986a.

Hart, J. E., G. A. Glatzmaier, and J. Toomre, Space-laboratory and numerical simulations of thermal convection in a rotating hemispherical shell with radial gravity, *J. Fluid Mech.*, *173*, 519–544, 1986b.

Johnson, C. L., and C. G. Constable, Persistently anomalous Pacific geomagnetic fields, *Geophys. Res. Lett.*, *25*, 1011–1014, 1998.

Jones, C. A., A. M. Soward, and A. I. Mussa, The onset of thermal convection in a rapidly rotating sphere, *J. Fluid Mech.*, *405*, 157–170, 2000.

Niu, F., and L. Wen, Hemispherical variations in seismic velocity at the top of the Earth's inner core, *Nature*, *410*, 1081–1084, 2001.

Olson, P., and G. A. Glatzmaier, Magnetoconvection and thermal coupling of the Earth's core and mantle, *Philos. Trans. R. Soc. London, Ser. A*, *354*, 1413–1424, 1996.

Sarson, G. R., C. A. Jones, and A. W. Longbottom, The influence of boundary region heterogeneities on the geodynamo, *Phys. Earth Planet. Inter.*, *101*, 13–32, 1997.

Siggia, E., High Rayleigh number convection, *Annu. Rev. Fluid. Mech.*, *26*, 137–168, 1994.

Stevenson, D. J., Limits on lateral density and velocity variations in the Earth's core, *Geophys. J. R. Astron. Soc.*, *88*, 311–319, 1987.

Sumita, I., and P. Olson, A Laboratory model for convection in Earth's core driven by a thermally heterogeneous mantle, *Science*, *286*, 1547–1549, 1999.

Sumita, I., and P. Olson, Laboratory experiments on high Rayleigh number thermal convection in a rapidly rotating hemispherical shell, *Phys. Earth Planet. Inter.*, *117*, 153–170, 2000.

Sumita, I., and S. Yoshida, Thermal interactions between the mantle, outer and inner cores and the resulting structural evolution of the core, *Core Dynamics, Structure and Rotation*, edited by V. Dehant et al., AGU, Washington, D.C., in press, 2002.

Sumita, I., S. Yoshida, M. Kumazawa, and Y. Hamano, A model for sedimentary compaction of a viscous medium and its application to inner-core growth, *Geophys. J. Int.*, *124*, 502–524, 1996.

Sun, Z.-P., G. Schubert, and G. A. Glatzmaier, Numerical simulations of thermal convection in a rapidly rotating spherical shell cooled inhomogeneously from above, *Geophys. Astrophys. Fluid Dyn.*, *75*, 199–226, 1994.

Tanaka, S., and H. Hamaguchi, Degree one heterogeneity at the top of the Earth's core, revealed by *SmKS* travel times, in *Dynamics of Earth's Deep Interior and Earth Rotation, Geophys. Monogr. Ser.*, vol. 72, edited by J.-L. Le Mouel, D. E. Smylie, and T. A. Herring, pp. 127–134, AGU, Washington, D.C., 1993.

Tanaka, S., and H. Hamaguchi, Degree one heterogeneity and hemispherical variation of anisotropy in the inner core from *PKP*(BC)-*PKP*(DF) times, *J. Geophys. Res.*, *102*, 2925–2938, 1997.

Tilgner, A., and F. H. Busse, Finite-amplitude convection in rotating spherical shells, *J. Fluid Mech.*, *332*, 359–376, 1997.

van der Hilst, R. D., and H. Kárason, Compositional heterogeneity in the bottom 1000 kilometers of Earth's mantle: Toward a hybrid convection model, *Science*, *283*, 1885–1888, 1999.

Walker, A. D., and G. E. Backus, On the difference between the average values of B_r^2 in the Atlantic and Pacific hemispheres, *Geophys. Res. Lett.*, *23*, 1965–1968, 1996.

Yoshida, S., and Y. Hamano, Fluid motion of the outer core in response to a temperature heterogeneity at the core-mantle boundary and its dynamo action, *J. Geomagn. Geoelectr.*, *45*, 1497–1516, 1993.

Yoshida, S., and E. Shudo, Linear response of the outer core fluid to the thermal heterogeneity on the core-mantle boundary, paper presented at the 7th SEDI Symposium, Study of the Earth's Deep Inter., Exeter, U.K., 2000.

Yoshida, S., I. Sumita, and M. Kumazawa, Growth model of the inner core coupled with outer core dynamics and the resulting elastic anisotropy, *J. Geophys. Res.*, *101*, 28,085–28,103, 1996.

Zhang, K., and D. Gubbins, On convection in the Earth's core driven by lateral temperature variations in the lower mantle, *Geophys. J. Int.*, *108*, 247–255, 1992.

Zhang, K., and D. Gubbins, Convection in a rotating spherical fluid shell with an inhomogeneous temperature boundary condition at infinite Prandtl number, *J. Fluid Mech.*, *250*, 209–232, 1993.

Zhang, K., and D. Gubbins, Convection in a rotating spherical shell with an inhomogeneous temperature boundary condition at finite Prandtl number, *Phys. Fluids*, *8*, 1141–1148, 1996.

P. Olson, Department of Earth and Planetary Sciences, Johns Hopkins University, 3400 N. Charles Street, Baltimore, MD 21218, USA. (olson@jhu.edu)

I. Sumita, Department of Earth Sciences, Faculty of Science, Kanazawa University, Kakuma, Kanazawa, Ishikawa, 920-1192, Japan. (sumita@hakusan.s.kanazawa-u.ac.jp)